

Manufacturing 3D Biomimetic Tissue: A Strategy Involving the Integration of Electrospun Nanofibers with a 3D-Printed Framework for Enhanced Tissue Regeneration

Aayushi Randhawa, Sayan Deb Dutta, Keya Ganguly, Tejal V. Patil, and Ki-Taek Lim*

3D printing and electrospinning are versatile techniques employed to produce 3D structures, such as scaffolds and ultrathin fibers, facilitating the creation of a cellular microenvironment in vitro. These two approaches operate on distinct working principles and utilize different polymeric materials to generate the desired structure. This review provides an extensive overview of these techniques and their potential roles in biomedical applications. Despite their potential role in fabricating complex structures, each technique has its own limitations. Electrospun fibers may have ambiguous geometry, while 3D-printed constructs may exhibit poor resolution with limited mechanical complexity. Consequently, the integration of electrospinning and 3D-printing methods may be explored to maximize the benefits and overcome the individual limitations of these techniques. This review highlights recent advancements in combined techniques for generating structures with controlled porosities on the micro–nano scale, leading to improved mechanical structural integrity. Collectively, these techniques also allow the fabrication of nature-inspired structures, contributing to a paradigm shift in research and technology. Finally, the review concludes by examining the advantages, disadvantages, and future outlooks of existing technologies in addressing challenges and exploring potential opportunities.

1. Introduction

Tissue engineering has evolved to apply scientific and technical concepts to the restoration and replacement of damaged or diseased organs. To enhance healthcare protocols, tissue

engineering employs a combination of cells, biochemical components, and engineered materials.^[1] A key challenge in this research lies in the generation of a patient-specific framework that accurately mimics the biological and physical characteristics, as well as the intricate hierarchies of native tissues. 3D printing, frequently referred to as additive manufacturing, has become a widely employed technique for the development of personalized and biomimetic scaffolds. This process involves layer-by-layer fabrication of the desired material.^[2] The versatility of 3D printing as a customized manufacturing process makes it a promising technique for various biomedical applications. This technique has persistently emerged from the design of small-scale and extensive 3D objects.^[3]

In contrast to traditional methods for simulating tissues, 3D-printed scaffolds exhibit well-regulated spatial biochemistry and geometry because this technique enables the highly organized assembly and deposition of numerous components, including polymer materials, cells, and

functional chemicals. 3D-printing techniques, such as stereolithography (SLA), digital light processing (DLP), and continuous liquid interface production, which rely on the photo-cross-linking principle, are the most widely used techniques for manufacturing tissue-specific scaffolds.^[4] Nevertheless, most of the existing 3D-printing techniques cannot generate the high-resolution fibrous structures required for building scaffolds for various tissues.^[5]

Electrospinning has been one of the most widely used techniques over the last few decades due to its ability to fabricate a range of fibrous (micro/nano) architecture with high porosity, surface functionalization, and tunable structural characteristics.^[6] Electrospinning is a reliable and straightforward approach that utilizes high voltage to generate fibrous structures with nanoscale dimensions and a significant surface area. It is an efficient and effective method for elongating and aligning polymer chains to create nanofibers that simulate the physical characteristics of a natural extracellular matrix (ECM). This provides a variety of attachment sites for cell growth and adhesion, thereby influencing cellular proliferation and morphological behavior.^[7] Although nanofibers provide a suitable basis

A. Randhawa, S. D. Dutta, K. Ganguly, T. V. Patil, K.-T. Lim

Department of Biosystems Engineering

Kangwon National University

Chuncheon 24341, Republic of Korea

E-mail: ktlim@kangwon.ac.kr

A. Randhawa, T. V. Patil, K.-T. Lim

Interdisciplinary Program in Smart Agriculture

Kangwon National University

Chuncheon 24341, Republic of Korea

S. D. Dutta, K.-T. Lim

Institute of Forest Science

Kangwon National University

Chuncheon, Gangwon-do 24341, Republic of Korea

 The ORCID identification number(s) for the author(s) of this article can be found under <https://doi.org/10.1002/smll.202309269>

DOI: 10.1002/smll.202309269

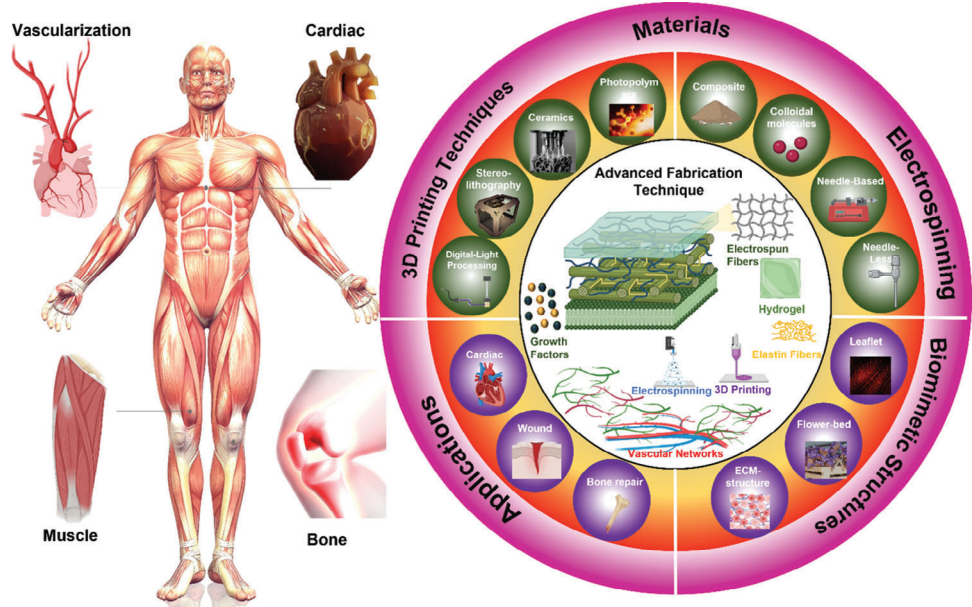


Figure 1. A schematic representation of the current study. Types of 3D printing and electrospinning techniques. Combined 3D printing and electrospinning strategies to produce biomimetic structures for tissue engineering applications.

for the administration and sustained release of peptides, drugs, and other bioactive substances by encapsulating them within the fibers or through surface immobilization, their limited mechanical properties constrain their applications in the biomedical field. To overcome the shortcomings of both 3D printing and electrospinning techniques, combining these methods enables the fabrication of highly porous structures with enhanced mechanical performance.^[8] The generation of advanced micro-nano fibers by employing electrospinning and 3D printing allows the generation of tissue-specific structures, overcoming the limitations associated with individual techniques. This review emphasizes recent progress in both techniques and the role of the materials used in creating tissue-specific structures. The integration of the two separate techniques and their importance in the fabrication of biomimetic structures are also discussed. Finally, this review summarizes the challenges and prospects. A schematic overview of this systematic review is presented in Figure 1.

2. Electrospinning

The technique by which a polymeric solution is transformed into fibrous structures under the influence of a strong electric field is known as electrospinning. The power supply used in electrospinning can be a direct current or alternating current (Figure 3a(i)). In traditional electrospinning machines, a syringe containing the spinning mixture is linked to the positive terminal, whereas the negative terminal is grounded to the collecting device.^[9] Once the syringe is filled with the polymeric solution and coupled to a high voltage, the droplet at the nozzle gets electrically charged, with the generated charges distributed equally at the droplet's surface. This cumulation of charge begins to alter the typical droplet shape produced by the surface tension, and the apex of the droplet acquires a cone shape, creating a "Taylor cone".^[10]

A narrow stream of the charged polymeric solution flows out through the Taylor cone when the strength of the electric field exceeds a certain threshold, where the repelling electrostatic force defeats the surface tension. The stream of the charged polymeric solution then undergoes whipping and stretching due to electrical fluctuations, creating a series of spiraling loops. These whipping and stretching fluctuations lead to the formation of long, narrow threads. Synchronously, the solvent evaporates, leaving solid polymeric threads stacked on the collector.^[11] In brief, the electrospinning method generally involves four successive steps: i) establishment of a Taylor cone or cone-like jet by electrically charging the droplet, ii) elongation of the jet in an uninterrupted straight line, iii) electric field-assisted thinning of the jet and formation of whipping instabilities (also called electrical bending instabilities), and iv) hardening and accumulation of the jet in the form of solid fibers onto the collector.^[12]

2.1. Modifications in Electrospinning Techniques

The electrospinning technique is simple and easy to operate in the laboratory, but increasing its output and accuracy remains difficult. Consequently, by altering the setup through the development of numerous needles in series, near-field electrospinning, and needleless electrospinning techniques, research has been conducted diligently to enhance the efficacy of the electrospinning process. In this section, we focus on the modifications of electrospinning techniques, including needle-based and needleless methods of producing nanofibers.

2.1.1. Needle-Based Electrospinning Method

The 3D single-needle electrospinning method provides the foundation for the multi-needle electrospinning technique, which

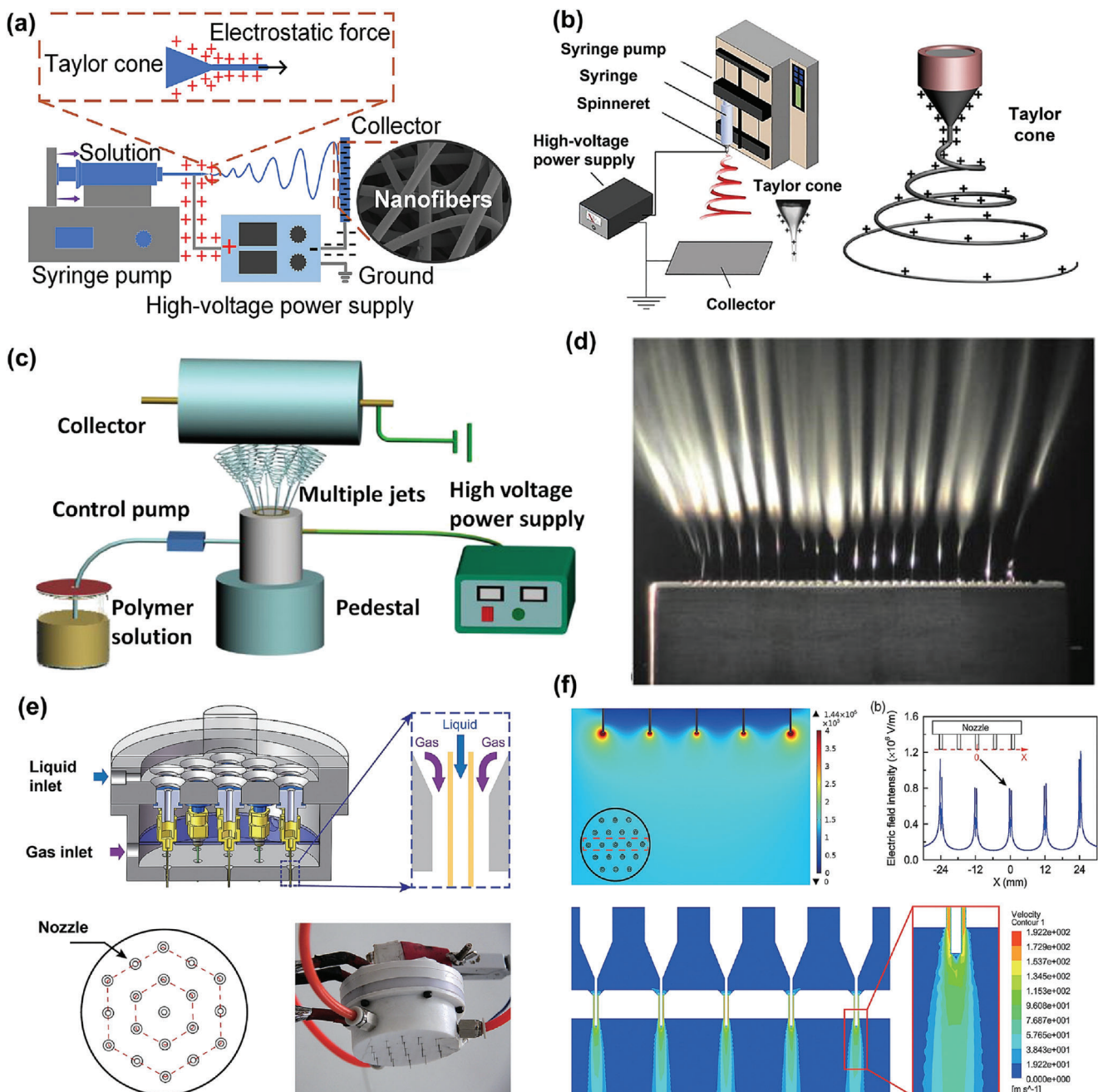


Figure 2. a) Basic horizontal electrospinning setup. Adapted with permission.^[27] Copyright 2017, Wiley and b) Vertical electrospinning setup. Adapted with permission.^[12] Copyright 2019, American Chemical Society. c) Schematic of a needle-less spinneret electrospinning apparatus. Adapted with permission.^[28] Copyright 2019, Elsevier. d) Multiple jets were generated with the needleless electrospinning setup at higher voltages. Adapted with permission.^[21] Copyright 2021, Wiley. e) Multiple-needle-based electrospinning setup, and f) the distribution of electric field at the nozzle tip during multi-nozzle spinneret for electrospinning. Adapted with permission.^[29] Copyright 2019, Wiley.

creates a matrix of orifices as a series of spinnerets organized in specific configurations.^[13] Depending on the application, various multi-needle configurations have been explored.^[14] Needle-based electrospinning involves horizontal and vertical methods (Figure 2a,b). Vertical electrospinning, also known as a top-down system, involves forming fibers on the gravity axis. The Taylor cone in the vertical method remains uninterrupted due to the

same direction as the gravitational and electrostatic forces. In the horizontal electrospinning system, the syringe tip and collector arrangement ensure that electrospinning occurs parallel to the ground. Gravity remains perpendicular to the electrical forces in this case. The Taylor cone direction in horizontal methods is distorted due to the perpendicular directions of electrical force and gravity.

Multi-Needle Electrospinning: Multi-jet electrospinning (also known as multi-needle) was created to solve the low efficiency of single-spinneret electrospinning.^[15] As the name suggests, multi-needle electrospinning uses multiple spinnerets to speed up fiber manufacturing. Multi-needle electrospinning can create specific composite mats by incorporating different spinning dopes—even incompatible polymers—into the spinnerets. With the increase in spinnerets, needle clogging worsens, thereby hindering the output. Thus, while performing multi-jet electrospinning, higher viscosity spinning dopes are typically more appropriate for needless electrospinning methods.^[16] Reduced efficiency may result from jet-to-jet repulsion among the spinnerets. In particular, the electric field and charged densities at the tip of the needle are considerably influenced by the multiple spinnerets. This change in the electric field and jet-to-jet repulsion results in irregular fiber structure and diameter distribution.^[15a] Needle arrangement, number, and spacing are crucial factors that must be considered when maximizing electric field uniformity during the multi-needle electrospinning technique (Figure 2e,f).^[15b]

Furthermore, generating fibers from several distinct materials at once is also possible using multiple needles, which encourages the development of membranes with greater functionality.^[17] Thus, the notion that the inner structures and chemical constituents of electrospun fibers can be tuned has inspired researchers. For instance, Loscertales et al. revealed that electrohydrodynamic stress caused the production of coaxial jets of non-miscible liquids with a micro/nanoscale diameter.^[18] For the coaxial spinneret structure to offer distinct paths for inner and outer solutions, the single needle was substituted by two coaxial capillaries, in which two passageways were linked to the two reservoirs.^[19] The capability to build delicate structures is one of the key benefits of the needle-based electrospinning method, and the generation of nanofibers primarily relies on the drafting impact caused by electric field force.^[20] Nevertheless, there is a significant barrier to the widespread use of this technique due to the complicated structure of the multi-needle electrospinning system.^[21]

2.1.2. Needleless Electrospinning

This electrospinning method has been developed to overcome the shortcomings of needle-based electrospinning systems. The primary objective behind the development of needleless electrospinning was to create an electrospinning setup with a high production level while avoiding the challenges posed by traditional electrospinning methods.^[22] The needleless method utilizes protrusions formed on the liquid's free surface to operate multiple jets simultaneously by applying high voltages, such as fiber generators, significantly enhancing manufacturing capacity (Figure 2c,d).^[23] The spinning dope is actively stirred as a high voltage is supplied during needleless electrospinning. The Taylor cone subsequently develops on the flat surface of the spinning dope as a consequence of the combined influence of the resultant electric field and stirred solution. The Taylor cone's tip produces polymer jets that move to the collector where nanofibers are formed. This method has effectively implemented needleless electrospinning for many fluid agitation tech-

niques, including disk, bubble, ball, coil, spiral, slot, and rotatory cones.^[22,24]

A previous study employed the “bubble electrospinning” method to utilize specific airflow to facilitate jet initialization from the free fluid surface.^[25] In bubble electrospinning, the agitation of the spinning dope involves compressed air to generate bubbles on the solution's surface. The resulting bubbles serve as the fiber producers and initiation sites for developing polymer jets. Advantageously, it has been demonstrated that this method can generate fibers of ≈ 50 nm and have an efficiency level that is a minimum of two orders of magnitude higher than that of conventional electrospinning.^[22] Nevertheless, bubbles, which are fragile and unstable, form the basis for fiber formation. The fiber shape is frequently of poor quality and might appear spherical or strip-like.^[26] Furthermore, fibers typically exhibit a wide variety of diameters and are inconsistent in structure. However, needless electrospinning offers an output 20–60 times greater than conventional electrospinning.^[24]

Although needless electrospinning has effectively increased the pace of fiber production, it has its challenges. Needless electrospinning encounters greater solvent evaporation because of greater exposure of the spinning dope to air. The resulting spinning dope's polymer content is consistently raised by this evaporation, which results in coarser fibers. Moreover, when trying to scale up or transfer this technique to a commercial setting, the accumulation of evaporated solvent could be hazardous, depending on the type of solvent employed.^[24,26]

2.2. Polymers for Electrospinning

Nanofibers have been produced via electrospinning from a variety of materials. Although polymeric materials are the mainstay of electrospinning, fibers can be generated from metals, ceramics, and inorganic chemical substances when a carrier polymer is present. The carrier polymer can then be retained or eliminated upon post-fabrication processing. The most frequently utilized materials are organic polymers, which come in suspension or melt form. Small particles can also be electrospun straight into nanofibers if they self-assemble and create enough chain entangling. As-obtained solutions have also been employed for electrospinning by adding nanoscale elements to polymer mixtures with diverse dimensions and topologies, such as nanorods, nanoparticles, nanowires, nanotubes, and nanosheets.^[12,30] Composite substances are electrospun promptly into nanofibers when paired with sol-gel processing.^[31] Brief descriptions of all these varying materials in the electrospinning or electrospun nanofiber setting are provided in the following subsections.

2.2.1. Organic Polymers

Most materials used in electrospinning are organic polymers, which occur as melts or solutions. For ease of reference, we refer to the corresponding techniques as melt and solution electrospinning. Due to their prevalence, numerous natural, synthetic, and partially synthetic polymers have been successfully electrospun into fibers. Robust electrospinning solutions can be made from polymers of all types, including homopolymers, copolymers, and

mixes. Mixed polymers combine two or more polymers instead of copolymers containing covalent bonding. Copolymers and polymer mixes are frequently used to achieve hybrid physical, chemical, and mechanical qualities. However, uniformity and reproducibility between batches must produce homogenous, uniform fibers with the expected structure. In theory, most naturally occurring polymers can be electrospun with the help of an appropriate solvent (for polymeric solutions) or by acquiring melts lacking thermal decomposition (for polymer melts).^[32]

Solution Electrospinning: In this electrospinning method, whipping instabilities cause a jet of the polymeric solution to be elongated, stretched, and thinned. As a result, the solvent rapidly evaporates, solidifying the jet and depositing tiny solid fibers onto the collector.^[33] Over a hundred distinct varieties of organic polymers comprising both synthetic and natural polymers have been extensively investigated. For commercial purposes, including environmental preservation, synthetic polymers such as poly(vinyl) chloride and polystyrene have been used to generate nanofibers. The selection of synthetic polymers generally occurs based on molecular force characteristics and thermal behavior. Thermoplastics such as polyesters, nylon-6, polyvinylidene fluoride (Figure 3a(iv)), elastomers such as polyglycerol sebacate and polyurethane, and thermosets including polymethyl methacrylate and polyurethane can be readily electrospun into nanofibers. Other synthetic polymeric compounds that are biodegradable and biocompatible, such as poly(lactic-co-glycolic acid) (PLGA) and poly-L-lactic acid (PLLA) (Figure 3a(ii)), as well as polycaprolactone (PCL) (Figure 3a(iii)), can be effectively electrospun into nanofibers and are currently being investigated as scaffolds for tissue engineering applications. Naturally derived biopolymer solutions have also produced nanofibers, including chitin, silk fibroin (SF), chitosan, DNA, dextran, collagen, alginate, and gelatin. Electroconductive polymers, such as polypyrrole and polyaniline, are employed to generate nanofibers with conductive properties. Table 1 presents a selection of available electrospinning techniques and materials.

Generally, several factors linked to the polymer, polymer solution, solvent, operation parameters, and environmental factors influence the achievement of electrospinning a polymer solution and the morphology and structure of the resulting nanofibers.^[34] The two critical prerequisites for efficient solution electrospinning are i) a polymer with a sufficiently higher molecular mass and ii) the selection and availability of an appropriate solvent to dissolve the polymers. The rheological and electrical properties of the solution are significantly influenced by the molecular mass of the polymer used. Due to the restricted chain entanglement, the low molecular mass results in beads instead of threads. The solvent's solubility factor is important in producing a homogenous polymer solution; however, a solvent with an elevated solubility parameter does not always produce an ideal solution for electrospinning.^[35] The vapor pressure and volatility of the solvent govern its evaporation rate, which determines the jet solidification rate. The elevated volatility is not ideal for fiber spinning, since the jet may instantly harden after leaving the spinneret. When the volatility is very low, the nanofibers remain moist after settling on the collector. The solvent's dielectric constant regulates the strength of the electric repulsion between the surface charges on the jet. The applied voltage

needed to produce a steady jet will rise as the dielectric constant increases.

The common solvents are chloroform, dichloromethane, dimethylformamide, acetone, tetrahydrofuran, dimethyl sulfoxide, trifluoroethanol, and hexafluoro-isopropanol. Due to the increased dielectric constant, water is not considered a desired solvent for fiber generation. Consequently, the electrostatic repulsion diminished. It may occasionally be required to combine various solvents to create the optimal mixture for electrospinning. Along with the molecular mass of the polymer and the kind of solvent, the spinnability of a polymer solution is highly influenced by the concentration and conductivity of electricity. To generate the fibers, a minimum concentration of electrical conductivity is necessary for the network entanglement to transition from electrospraying to electrospinning.^[36] Below this concentration, the jet splits into droplets, and small particles or polymeric beads are produced instead of continuous filaments, a procedure known as electrospray. This is because the interactions in the chains of polymers are too weak to withstand Rayleigh's instability. Once the concentration rises, the jet stops dispersing, the morphology of the beads transforms from circular to spindle-like, and eventually, uniform fibers form due to an upsurge in viscosity and chain entanglement.

Nevertheless, overcoming the viscoelastic force will be challenging if the concentration is excessively high, and no jet will emerge. Reducing the concentration encourages the emergence of thinner filaments within a reasonable range. Nevertheless, the polymer concentration also impacts the surface tension and viscosity of the solution, and these parameters affect the shape and dimensions of the resulting fibers. The manufacturing of thinner fibers is generally favored by reducing surface tension and viscosity. However, this can also be accomplished by adding a surfactant instead of decreasing the polymer concentration.^[37] If the viscosity of the solution is very high, the solution ejection from the spinneret becomes challenging, and if the solution has low viscosity, no fiber will be generated. Electrospinning is difficult for completely insulating solutions because their low conductivity prevents the transmission of charges from their interior to their surface. However, reduced electrostatic repulsion makes it difficult to produce a Taylor cone or initiate bending instability if the solution is excessively conductive, since surface charges cannot build up on conductive jets.^[38] Owing to the jet's significant bending, a rise in conductivity will only encourage the development of thinner fibers within a certain range. Incorporating ionic substances, including mineral acids and salts, into a solution of polymers is a reliable method for enhancing conductivity.^[39]

Melt Electrospinning: Several polymers, particularly polypropylene and polyethylene, are hard to dissolve in suitable liquids for electrospinning solutions. Under these circumstances, these polymers can be electrospun directly from melts into fibers.^[49] A schematic of the common melt electrospinning apparatus at different critical translation speeds is shown in Figure 3b(i–vii).^[50] The typical workflow of new-generation melt electrospinning using novel polymers comprises three main steps: i) parameter assessment, ii) application, and iii) dimension-dependent design. In assessment, crucial variables are changed, preferably digitally, to determine their precise influence on the results of melt electrospinning.^[51] PCL (Figure 3c) is typically preferred as a readily flexible polymer substance for

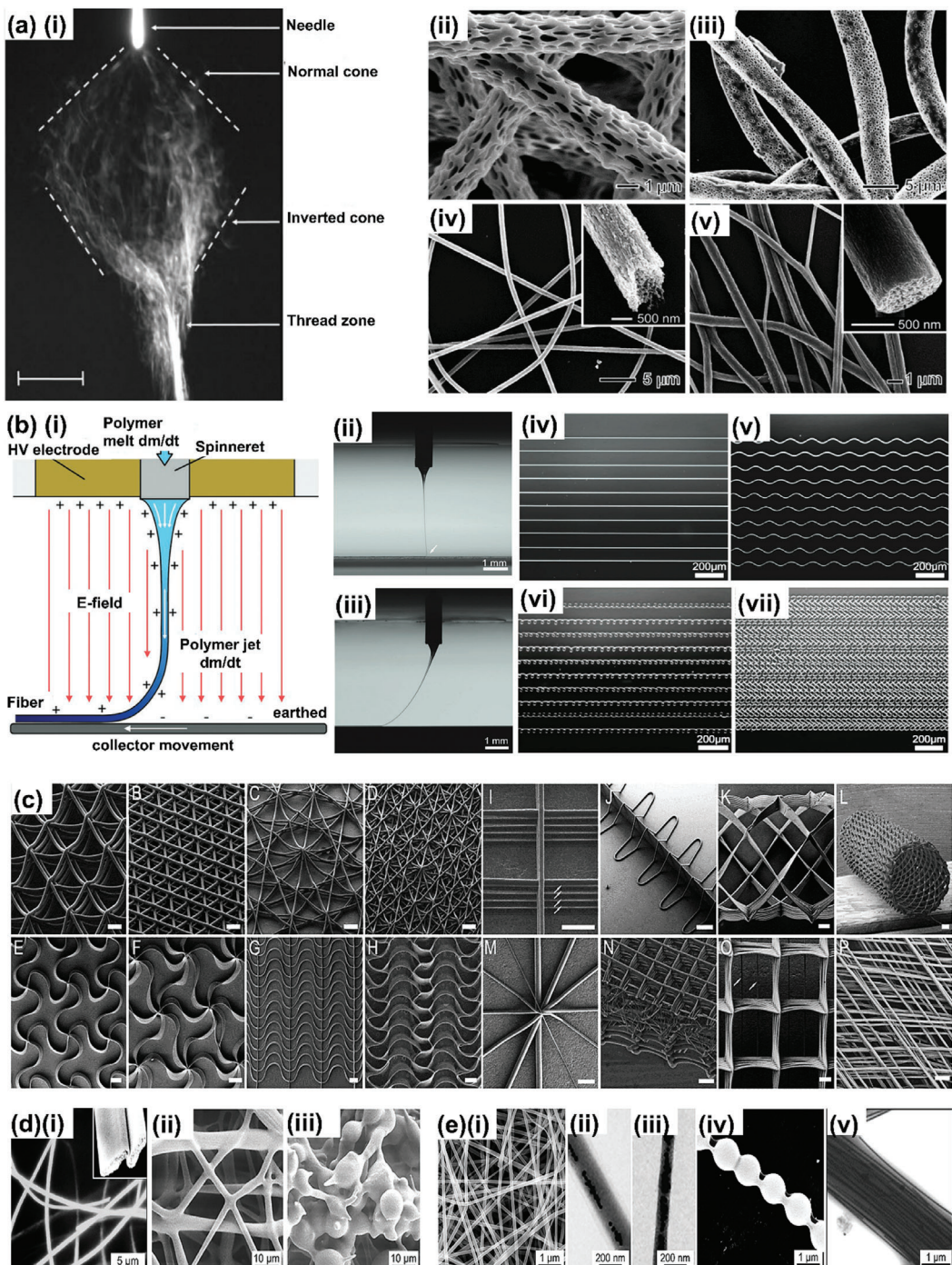


Figure 3. a) (i) Depiction of the jet formation during electrospinning with alternating current. Adapted with permission.^[12] Copyright 2019, American Chemical Society. a) SEM images of the electrospun fibers of (ii) PLLA, (iii) PCL, (iv) PAN, and (v) PVDF organic polymers, respectively. Adapted with permission.^[34b] Copyright 2017, American Chemical Society. b) (i) Schematic of melt electrospinning of a stable jet and electrospinning of molten jet onto a substrate in equilibrium so that the feed rate to the spinneret matches that of high voltage stabilized polymer jet to avoid fiber pushing. (ii) Images of a PCL MEW jet direct-written at the critical translation speed (CTS) on a flat collector with the jet “heel” (white arrow) indicated and (iii) above the CTS on a cylindrical mandrel. (iv) a series of fibers deposited at increasingly lower collector speeds, starting above the CTS, v) x0.75 CTS, vi) x0.35 CTS, and vii) x0.10 CTS, c) SEM images of the several melt electrospun PCL scaffolds. Adapted with permission.^[72] Copyright 2019, Wiley. d) SEM image of the electrospun (i) colloidal particle such as LiCoO₂ fibers, (ii) small molecules such as lecithin fibers morphology, (iii) formation of lecithin droplets after electrospinning a solution of lecithin. Adapted with permission.^[72] Copyright 2019, Wiley. e) (i) SEM images of the electrospun composite nanofibers comprised of PVP and Ti(OiPr)₄ solution, (ii-iii) TEM images of the PVA-Ag nanoparticle composite nanofibers, (iv) SEM images of the composite nanofiber of PVA and SiO₂ particles showing necklace-like structure, (v) TEM image of a composite nanofiber obtained by electrospinning of PVP and Ag nanowire solution. Adapted with permission. Copyright 2019, American Chemical Society.^[12]

Table 1. Lists various electrospinning techniques and materials for generating micro/nanofibers for tissue engineering applications.

Electrospinning method	Material	Properties	Application	References
Needle-based electrospinning	Polyethersulphone, bioactive glass nanoparticles	Improved proliferation and progenitor adhesion, phenotypic maintenance of CD34+ cells	Bone regeneration and drug delivery	[40]
	Alginate	Highly bioactive, biocompatible and bio-adhesive	Wound healing, skin regeneration	[41]
Solution electrospinning	Hyaluronic acid	High mechanical strength, macrophage polarization, infiltration, and recapitulating ECM microenvironment	Soft tissue reconstruction, myofibroblast differentiation	[42]
	Polyether polyurethane	High mechanical strength and biocompatibility	Tendon, ligament regeneration, wound healing	[43]
	Polycaprolactone-gelatin-carbon nanotube	High mechanical strength, electroconductive	Cardiac and neural tissue engineering	[44]
Wet electrospinning	Polycaprolactone, Silk fibroin	High mechanical strength and cytocompatibility	Bone remodeling and wound regeneration	[45]
	Polyvinyl alcohol, melamine formaldehyde	Water resistant, high stability	Filtration, drug administration	[46]
Needleless electrospinning	Poly-L-lactic acid, polypyrrole	Highly electroconductive, adhesive, and biocompatible	Cardiac regeneration	[47]
Monoaxial electrospinning	Furfuryl-Gelatin	High biocompatibility, superior elastic modulus	Cardiac tissue engineering	[48]
Co-axial electrospinning	Polycaprolactone-gelatin-carbon nanotube	High mechanical strength, electroconductive	Cardiac and neural tissue engineering	[44]

highly efficient fabrication and iterations. The dataset produced, either manually or through software for jet visualization, is next examined for operational stability, beginning with regulating the mass flow rate to get rid of fiber pulsation.^[52]

After being released from the spinneret, due to the heat exchange between the jet and the medium (usually air), the jet cools and hardens to produce fibers in a molten state. Due to the electrohydrodynamic consequences, the heat exchange rate can significantly increase when an electric field is present.^[53] The air near the outer edge of the jet can be favorably ionized—resulting in a positively charged corona expulsion—when the edge of the spinneret and collector is exposed to the positive potential segregated by a dielectric component, i.e., molten jet and air.^[54] The applied voltage must be kept above the corona emergence, lowering the air gap collapse voltage. The heat exchange rate can be increased by several magnitudes when the corona voltage disturbs the thermal barrier connecting the jet and the air. Due to the rapid “freezing” and cooling of the jet brought on by electrohydrodynamic quenching, the jet’s amount of stretching is significantly reduced.^[55]

In contrast to solution electrospinning, melt electrospinning significantly reduces the whipping instabilities of the jet.^[56] This variation can be mainly attributed to the special characteristics of a polymer melt, which include (i) its ability to conduct electricity, which generally falls less than 10^{-10} S m⁻¹, and (ii) its viscosity, generally between 40 and 200 Pa s⁻¹. As a result, the molten jet has fewer surface charges, reducing whipping instability. The whipping instabilities can be further suppressed when the temperature of the jet falls below the glass transition tem-

perature of the polymeric material, and more intense electrostatic repulsion is needed to compensate for the viscoelastic force. As a result, the jet typically proceeds in a straight direction and is thinned by the electrostatic force produced by the surrounding electric field.^[57] The jet bends during compression, and the fibers twist over the midline during accumulation over a stationary collector. The fibers deposited on the collector do not prevent incoming new fibers. Melt electrospinning generates fibers that are typically thicker than the fibers produced with solution electrospinning due to the absence of solvent evaporation and whipping instabilities. In melt electrospinning, only a small proportion of commercially available polymers have been effectively investigated.^[56] The polymer must undergo a glass transitioning step that involves melting at a temperature with no thermal deterioration. As a result, proteins, thermally unstable polymers, and thermoset polymers cannot be spun by melt electrospinning. Thermoplastics like polyurethane, PCL, polylactide, and PLGA are the most commonly utilized polymers.^[12]

2.2.2. Colloidal Particles

In a colloid comprising a continuous phase, a medium of suspension, and a dispersed phase, the suspended particles are suitable for electrospinning when there is enough entanglement between the particles to keep the jet as a constant structure. A classic example is the electrospinning of aged inorganic sols possessing spinnable viscosities produced by the breakdown and condensation of metal salts or alkoxides. A stable electrospinning method

requires a particular dimension of the colloidal particles and cross-linking between them, with viscosity being a crucial factor in defining the diameter of the fiber. In a standard approach, a silica sol was made using ethanol, tetraethyl orthosilicate, distilled water, and hydrochloric acid, which was then stirred at 80 °C for 30 min.^[58] Silica fibers with diameters between 0.4 and 1 μm were obtained shortly after electrospinning. Likewise, silica nanofibers with a diameter smaller than 400 nm were created by modifying the aged sols' characteristics.^[59] In another investigation, electrospinning was done using an aged sol made from cobalt acetate, lithium acetate, citric acid, and distilled water.^[60] The electrospun fibers were then calcined to produce LiCoO₂ fibers with diameters between 0.5 and 2 μm (Figure 3d(i)). The transmission electron microscopy image shows that the fiber comprises homogenous LiCoO₂ nanoparticles with a 20–35 nm diameter. Ceramic fibers comprised of oxides, such as NiO, Co₃O₄, and a combination of ZnO and Al₂O₃ were synthesized using the sol–gel technique.

Nevertheless, the resulting fibers often had a diameter greater than a few micrometers. The difficulty in properly managing the rheological characteristics of a sol also makes it difficult to manage the size and homogeneity of the fibers.^[61] High concentrations of metal nanoparticles in a solution provide a spinnable mixture that can be used for electrospinning. In one study, Ag nanoparticles (40 ± 5 nm) were dissolved in ethylene glycol with a concentration of 50 weight%. The Ag nanoparticles in the solution aggregated and became electrically responsive, resulting in Ag nanofibers with an estimated diameter of 338 ± 35 nm following electrospinning and thermal processing at 150 °C in air. However, the difficulty of making extremely concentrated metal nanoparticle solutions limits this study's potential.^[62]

2.2.3. Small Molecules

Small molecules can be electrospun into fibers directly if the chain entanglement is strong enough to maintain the electrified jet and prevent Rayleigh's instability. In the electrospinning of small molecules, chain entanglement plays a key role because it can regulate molecular mobility and prevent the independent motion of molecule segments. By improving the chain entanglement, Rayleigh's instability can be reduced, and a stable jet can be maintained.^[63] Under ideal circumstances, small molecules can self-assemble under the influence of suitable solution conditions, for instance, via anionic and non-anionic noncovalent bonds, which helps attain the adequate chain entanglement required to electrospin fibers. Small molecules such as phospholipid amphiphiles, tetraphenyl-porphyrin, and mono- and dipeptides can be easily electrospun.^[63,64] Some small molecules, including phospholipids, show entanglement characteristics in their melts, forming continuous fibers. For instance, a phospholipid named 1-palmitoyl-2-oleoyl-sn-glycero-3-phosphoethanolamine, with a molecular mass of 718 g mol⁻¹, produces significant aggregates during its melt.^[65]

The presence of sufficient intramolecular interactions within a lecithin solution, composed of a 70:30 weight% mixture of chloroform and dimethylformamide with a concentration of

43 weight% (exceeding the critical micelle concentration), results in the generation of continuous fibers with an average diameter of 2.8 μm (Figure 3d(ii,iii)). In contrast, particles are produced from the solution with a concentration corresponding to the critical micelle concentration. Furthermore, an increase in concentration (50 weight%) results in the thickening of fibers (diameter of 5.9 μm). Likewise, bioactive peptide amphiphiles and Gemini surfactants have also been electrospun directly to produce fibers in a micrometer scale diameter.^[66] Cyclodextrin derivatives contain doughnut-shaped glucopyranose rings and can develop aggregates by hydrogen bonding, resulting in a highly viscous solution with properties like a viscoelastic solid.^[67] The electrospinning of a solution containing 120% (w/v) hydroxypropyl-cyclodextrin in dimethylacetamide produced fibrous structures ranging from 0.4 to 1.8 μm. Since a small molecule cannot generate a stable intramolecular interaction to achieve the necessary chain entanglement, incorporating carrier polymers into the polymer mixture can create stable interactions, which are further eliminated by post-fabrication techniques such as heat or solvent treatment. In situ polymerization techniques, including photopolymerization, are additional approaches for manipulating small molecules into fibers.^[68]

2.2.4. Composites

Modern fibrous components are often created using composite mixtures of polymers that follow sol–gel chemical engineering concepts. Composites are generally produced by incorporating nanoscale molecules and sol–gel substrates into a polymeric solution and have been widely investigated in solution electrospinning. Polymer–polymer composites can be prepared by adding polymers with various physicochemical properties to form unique composites with different characteristics, including customized biocompatibility, degradability, and mechanical stability. Incorporating colloids into a polymeric solution can immobilize nanoscale particles in a fibrous architecture. Colloids serve as excellent models of electrospun structures made with polymer–particle composites, depending on the molecular aggregation that occurs in the solution during electrospinning. Adequate particle distribution and entanglement allow stable maintenance of the polymer jet, which in turn allows the formation of composite fibers.^[12] When using the sol–gel precursor, limiting the sol–gel reaction rate in the stock solution is important. The precursor sol–gel processes, such as condensation, gelation, and hydrolysis, begin in the jet after contact with the air.^[69] The efficiency of the sol–gel processes in the jet is significantly influenced by the type of precursor used.^[69a] Quick gelation produces a less flexible jet, forming thicker fibrous structures, whereas swift hydrolysis frequently blocks spinnerets. Metal salts, such as nitrates, alkoxides, acetates, sulfates, and chlorides, are frequently used as precursors. Additives, such as hydrochloric acid, acetic acid, and propionic acid, are required to maintain the stability of the precursor solution and provide a steady electrospinning process.^[58,70] The viscosity of the polymer solution is a key factor in the stretching and extension of the jet and can be regulated by adjusting the polymer and precursor concentrations. Salts such as (CH₃)₄NCl and NaCl are employed to enhance

electrical conductivity for the development of thinner fibrous structures.

Furthermore, a controlled environment around the jet is crucial. Usually, an environment with reduced humidity and solvent vapor significantly slows gelation and hydrolysis rates, eventually resulting in continuous electrospinning.^[61] By adjusting these parameters, the morphology and diameter of the electrospun fibers can be reduced by up to several nanometers. The dispersion of nanomaterials in a polymeric solution by ultrasonication and intense stirring allows for the preparation of composites utilized in solution electrospinning. Nanoparticles fabricated with metals, such as Au, Ag, and TiO₂, as well as metal-organic framework substances, carbon nanotubes, Ag or Au nanowires, graphene nanosheets, and clay tablets are among the most frequently used nanomaterials. In this context, the electrospinning of SiO₂ particles networked with polyvinyl alcohol fibers results in the generation of necklace-shaped structures (Figure 3e(i–v)).^[71]

3. 3D-Printing Techniques

3.1. SLA

SLA is one of the most widely used 3D-printing techniques. Despite being the earliest and oldest, it is also the most popular because it produces objects with intricate geometries and smooth surfaces, owing to its excellent printing resolution. The first SLA-based 3D-printing process, a subset of vat photopolymerization, was invented and patented by Charles Hull in 1984. The term SLA consists of two words: “stereo” meaning solid and “lithography” meaning light or photo. SLA is characterized by the process of creating solid materials in the presence of light. This technique employs photopolymerizable materials, indicating that the material solidifies when exposed to a specific wavelength of light that controls the structure’s shape and size.^[73]

In an SLA system, a coherent illumination source, usually a UV-emitting laser, is used to allow polymerization of the liquid resin material. One of the key benefits of this technique is the high spatial accuracy provided by a concentrated laser beam. In SLA, light exposure is performed sequentially by scanning a laser beam across the surface of a photoresponsive material. The rate at which the laser beam is scanned and the dimensions of the illuminated region define the period required to obtain one slice of the construction.^[74] The curing depth is affected by the exposure dose, such as the illumination time and light intensity, which may explain the rare use of grayscale capability in actual applications. The most laborious procedure in SLA does not involve laser scanning but the deposition of a fresh film of photosensitive material, in which the viscosity of the material plays an important role. Solvents or nonreactive additives can control the viscosity of photosensitive polymers, which are commonly known as photopolymers. Figure 4a,b(i,ii) depicts the photopolymerization of polymers, such as polyamic diacrylate ester, to generate a complex 3D structure using the mask-projection micro-SLA technique.^[75] With the emerging field of SLA, it is possible to develop an improved enzyme immobilization carrier that partially fulfills the requirements for commercial enzyme catalysis.^[76]

3.2. DLP Printing Technology

Conventional 3D-printing techniques have recently undergone a significant change, primarily due to DLP-dependent 3D-printing methods, which have substantially improved production speed and resolution.^[74] DLP projects the image of an object’s cross-section onto a photosensitive resin using a projector similar to that utilized for business presentations. This technique allows for controlled image generation and printing accuracy. It has been over 20 years since the introduction of the DLP technique. Figure 4c(i) presents a schematic of a typical DLP printer, showcasing the opportunities and challenges offered by UV and visible light. An optical semiconductor, also known as a DLP chip or digital optical microscope, is the fundamental component of the DLP technique, originally invented by Dr. Larry Hornback (1977) and manufactured by Texas Instruments in 1996.^[78] Modern, sophisticated electronic DLP devices and their accessories are known as DLP technologies. Figure 4c(ii) depicts the process of visible light curing during DLP printing, which involves a general mechanism of oxidative quenching for a three-component system with the structures of photo-initiators and photo-redox catalysts involved during the process.^[77] The flipping time of the DLP device’s microscope can approach several periods per second, displaying gray shades of 1024 pixels and converting the received image and video signals into a detailed grayscale picture. As a result, DLP printing offers substantial printing precision and can produce printed structures as small as 50 μm in dimension. The DLP printer employs an LED light source with a wavelength of 405 nm because UV light cannot be used to print semiconductor materials. Plane exposure is used in DLP printing; however, the exposure region is constrained.^[79]

DLP printing has been used to manufacture complex structures, such as highly stretchable photopolymers, luminous 3D objects, customized nerve-directing conduits, reprogrammable thermosets, organic and inorganic composites, and conductive electrical constructs, among others.^[74] Free-radical photopolymer resins are typically used in DLP 3D-printing systems. This printing technique avoids cationic photopolymerization because the cationic photo-initiator seldom functions under 405 nm irradiation. A few cationic photo-initiators perform their function upon irradiation with 405 nm light, but their high cost limits their use. Furthermore, DLP printers do not use sufficient illumination to photolyze cationic photo-initiators, which prevents them from inducing photopolymerization.^[80] The primary advantages of a DLP printing system are its high precision and accuracy.^[81] Nevertheless, the dimensions of the projection are constrained to ensure high precision. Hence, it can only print structures with smaller sizes.^[82]

3.3. Inkjet Printing

Inkjet printing is one of the most well-known 3D-printing techniques and has garnered significant interest in accurate 3D manufacturing.^[83] With high resolution and efficacy, this technique allows the deposition of biomolecules, polymers, electrical components, and various living cells using a non-contact method.^[84] Inkjet printing techniques can be

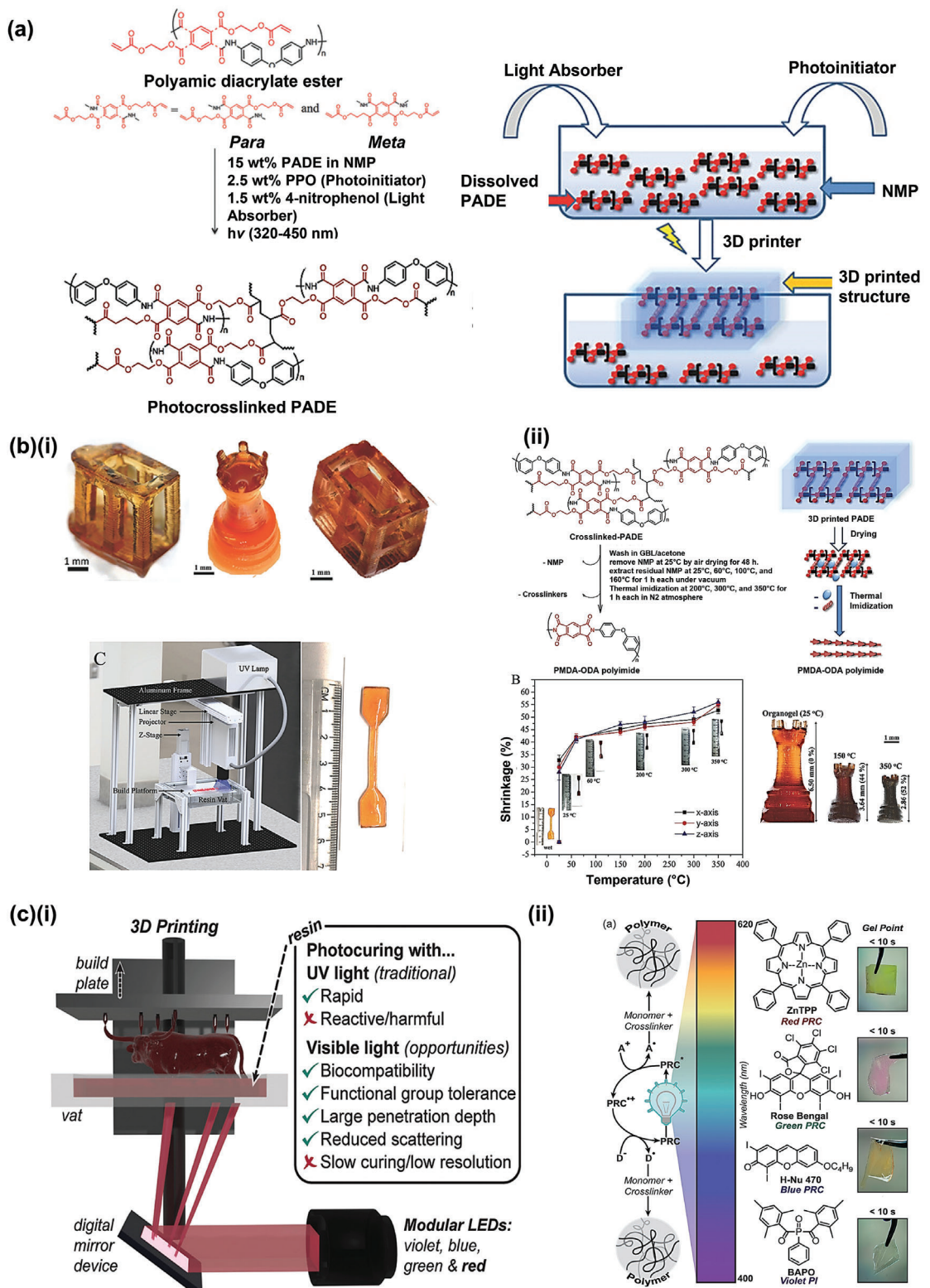


Figure 4. a) Chemical structure of the photopolymer PADE used in SLA-based printing system. b) (i) Photographs of the complex 3D structures printed with the SLA printers. b) (ii) Steps involved in the post-printing process of 3D-printed structures. (ii) The dimensional shrinkage of the structures during the post-printing process. Adapted with permission.^[75] Copyright 2017, Wiley. c) (i) The schematic illustration of the DLP printer with its benefits and opportunities. c) (ii) Visible-light photocuring during DLP printing and its mechanism of a three-component system. Adapted with permission.^[77] Copyright 2020, American Chemical Society.

Table 2. List of various 3D printing techniques and materials for generating tissue-specific structures.

3D Printing method	Materials	Properties	Application	References
Sterolithography	Poly (propylene fumarate)/diethyl fumarate,	Fabrication of complex internal features,	Bone tissue engineering	[104]
	Poly (propylene fumarate)/diethyl fumarate/Hyaluronic acid	Patterning of proteins, growth factors, and cells		
Extrusion-based printing	Nano biphasic calcium phosphate/Polyvinyl alcohol	Improved biocompatibility, biological activity, and osteogenic differentiation	Bone remodeling, articular cartilage	[105]
	Polylactic acid/Fe ₃ O ₄	Biodegradable shape-memory occluders promoting cell proliferation and rapid endothelialization		
Fused-deposition modeling	Poly-L-lactic acid, Polycaprolactone/poly ethylene glycol, Polyurethane	Improved biological performance, mechanical strength, and osteogenic differentiation	Bone remodeling, antibacterial properties	[107]
	Polycaprolactone/Poly (glycerol sebacate)	Improved elasticity, mechanical properties, and inhibition of left ventricular dilation		
	Polycaprolactone	Enhanced synchronous beating, cellular adhesion, and proliferation of cardiomyocytes	Cardiac tissue engineering	[108]
Solution and melt-based electrohydrodynamic printing			Cardiac tissue engineering	[108, 109]
Photolithography	SU-8 (epoxy polymer)/Polycaprolactone	Thermo-responsive and improved mechanical properties	Drug delivery and tissue engineering	[110]
Digital light processing	Polycaprolactone methacrylate	Shape-memory recovery and high mechanical properties	Development of endoluminal device for respiratory tract	[111]

divided into two categories based on the ink droplets developed in the printer: i) continuous inkjet printing and ii) drop-on-demand inkjet printing.^[85] In continuous inkjet printing, a liquid stream emerges from the nozzle because of Rayleigh–Plateau instability.^[86] Nonetheless, due to the printer's intricacy, bioink waste, and possible material contamination, printing with a continuous inkjet printer is limited.^[87]

Compared to continuous inkjet printing, drop-on-demand inkjet printing achieves greater accuracy and effectiveness by ejecting droplets only when required.^[88] In addition, the general structure of the device is streamlined, making it an excellent choice for 3D printing in laboratories and industries. Furthermore, it is possible to customize the drop-on-demand printer with several nozzles and a diameter range as low as 18 μm .^[89] The ejected droplets with diameters less than 30 μm facilitate the fabrication of 3D constructs with a higher resolution.^[87b] Drop-on-demand printers use nozzles with piezoelectric, thermal, and electrostatic actuation to deposit droplets for printing.^[88,90]

3.4. Materials Used in 3D Printing

The choice of material depends on the manufacturing process. Different polymers originate from natural and synthetic sources and develop structures with well-defined characteristics. Additionally, 3D printing allows the fabrication of 3D constructs with complex geometries for specific applications in tissue engineer-

ing, biosensors, and biorobots, among others. Materials used for 3D-printing applications vary from photopolymer ceramics to thermoplastics and concrete. The commonly used materials and printing techniques are listed in Table 2.

3.4.1. Photopolymers

Vat photopolymerization is an additive manufacturing process that utilizes light of a specific wavelength (UV light) to cure the photopolymers present in the vat via light-induced polymerization, allowing layer-by-layer fabrication of 3D structures. 3D-printing techniques, such as SLA and DLP, rely on the principle of photopolymerization. In these techniques, printing occurs inside a UV-responsive liquid-resin chamber, where a UV light source locally cures the polymer resin along the projected or printed segments to create a solid structure. The second resin layer is then cured on top of the first layer as the printing advances in the Z-direction. Photopolymers show very high sensitivity to UV light, and cross-linking occurs after exposure to UV light. Generally, following the printing process, printed structures require liquid or ultrasonic baths to remove excess untreated resin residues.^[91] Most photocurable constituents include functional monomers, oligomers, photo-initiators, and other additives.^[92] Oligomers make up most of the photocurable resins (with a weight ratio of 70–80%), and their properties significantly impact the overall efficacy of printing. Polymerization commences upon activation of the photo-initiator. It is crucial to determine the physical manufacturing efficiency,

such as the curing rate and resin viscosity, as well as mechanical characteristics, such as hardness and shrinkage rate.^[93] Acrylate- and methacrylate-based polymers, such as gelatin methacrylate (GelMA), chitosan methacrylate, hyaluronic acid methacrylate, and collagen methacrylate, are most commonly used because of their rapid reaction rates, adjustable mechanical characteristics, and long-range stability.^[74,94] Figure 5a illustrates the Pt(IV)-triggered photopolymerization of the GelMA construct for post-operative cancer therapy. A microfluidic printing technique was used to create the Pt-GelMA framework from a solution containing GelMA and Pt(IV). In this context, the manufactured structure of Pt(IV) not only exhibits the potential for light-driven reduction to Pt(II) for effective tumor eradication but also triggers the production of N3· required for the cross-linking of GelMA.^[95] However, these monomers exhibit significant volume shrinkage issues during chain expansion in photopolymerization, leading to the production of extremely brittle objects and restricting their use in further applications. The production of alkyne carbonate molecules with improved toughness has been demonstrated to have comparable curing rates, substantially greater conversion, and lower cytotoxicity than acrylates.^[96] Several alkyne-carbonate-based molecules engage in thiol-yne photochemical processes with various thiols, facilitated by a photo-initiator following exposure to blue light at a wavelength of 465 nm in a 3D printer. Notably, network uniformity and decreased shrinkage during the thiol-yne photopolymerization of alkyl carbonates result in the generation of polymer compounds with adequate toughness. The degradability of the resulting polymer compounds could be selectively controlled by altering the amount and type of thiol monomers. Alkyne carbonate resins are potential candidates for the 3D fabrication of rigid biomaterials, such as bone frameworks.^[96]

3.4.2. Ceramics

Ceramics are an intriguing family of materials used in chemical manufacturing because of their strong chemical and thermal resistance and ability to incorporate catalytically active constituents.^[97] There are two primary strategies for 3D printing ceramics using high-resolution SLA: i) the use of a preceramic solution or ii) the generation of photocurable composites. Ceramic particles (preferably nanoparticles) have been mixed with a photocurable binder matrix to create photocurable composites. Similar to fused silica glass, these composites can be 3D printed using SLA to produce a strong ceramic after being subjected to thermal sintering (Figure 5b). Several chemically and thermally robust ceramics, such as alumina, can be printed using SLA.^[98] Preceramic polymers were introduced in 1960. Following heat treatment, pyrolysis of organosilicon polymers results in several useful ceramics for chemical production, such as SiOC.^[99] Bioceramic scaffolds composed of calcium silicate, bioactive glasses, and calcium phosphate are gaining attention in tissue engineering because they resemble natural bone constituents. These ceramics play important roles owing to their potential bioactivity, osteoconductivity, hydrophilicity, biocompatibility, and osteo-inductivity.^[100] Various 3D-printing methods, such as selective laser sintering, SLA, and fused deposition modeling, rely on ceramics for various biomedical applications. These

printing techniques vary depending on their principle of fabrication; for instance, selective laser sintering utilizes a sintering approach to sinter the particles, SLA uses UV irradiation for layer-by-layer fabrication, while fused deposition modeling involves the layer-by-layer deposition of filaments on a workbench to create scaffolds.^[101] A CaSiO₃ ceramic made of bioactive materials has been investigated for bone regeneration.^[102] Immersion of these biomaterials in simulated body fluid results in the formation of a carbonated hyaluronic acid layer with a bone-like appearance on the surface, which creates a strong chemical link between the bone tissue and the surrounding biomaterial.^[103]

3.4.3. Shape Memory Polymers (SMPs)

SMPs are materials that respond to different external stimuli. SMPs are frequently used in 3D printing to produce soft robotic systems. These materials retain their original shape and can revert to their original shape after being manually distorted into temporary structures. Despite many distinct shape memory actuators activated by thermal, light, or chemical stimuli, thermally responsive SMPs have been investigated extensively.^[112] Two crucial physicochemical conditions must be fulfilled for a polymer to exhibit a thermal shape memory response: chemical or physical cross-linking. This process establishes the permanent structure and melting temperature, functions as a molecular switch, and determines the temporary shape. In the last decade, SMPs have been developed for 3D-printing techniques, such as fused deposition modeling, vat polymerization, and poly jets.^[113] Figure 5c(i) shows the chemical structures of tert-butyl acrylate and di(ethylene glycol) diacrylate, which are SMPs that work on network formation between the tert-butyl acrylate monomer and di(ethylene glycol) diacrylate crosslinker during UV photopolymerization.^[94] Most research on 3D printable SMPs aims to enhance shape memory response, mechanical properties, and melting temperature control. SLA and poly jets are the two 3D printing processes primarily utilized to develop printable SMPs.

In the poly jet method, computer-aided techniques enable controlled deposition of distinct materials at a single voxel. The characteristics of the printed object can be regulated and tailored at the voxel stage. Wu et al. fabricated multiple digital SMPs using 3D printing, specifically Verowhite + TangoBlack. They aimed to develop a structure with multiple morphological characteristics according to temperature conditions.^[114] An intriguing method for 3D-printed SMP actuators was illustrated by Ding et al., where a bilayer elastomeric SMP actuator was printed in its temporary shape, and, upon heating, the permanent structure was recovered. This was a novel phenomenon, and the bilayer framework exhibited a shapeshift.^[113b] SMPs often exhibit irreversible movement, but the typical actuation cycle involves transitioning from a transient shape to a fixed shape. Thus, the object must be manually reconfigured into a temporary configuration using an external force to enable further actuation to occur. These drawbacks limit the application of these materials in soft robotics. Recently, reversible SMPs have been developed to overcome this problem. The combined method involves merging the mechanism of the SMP with another actuation process, which is a primary

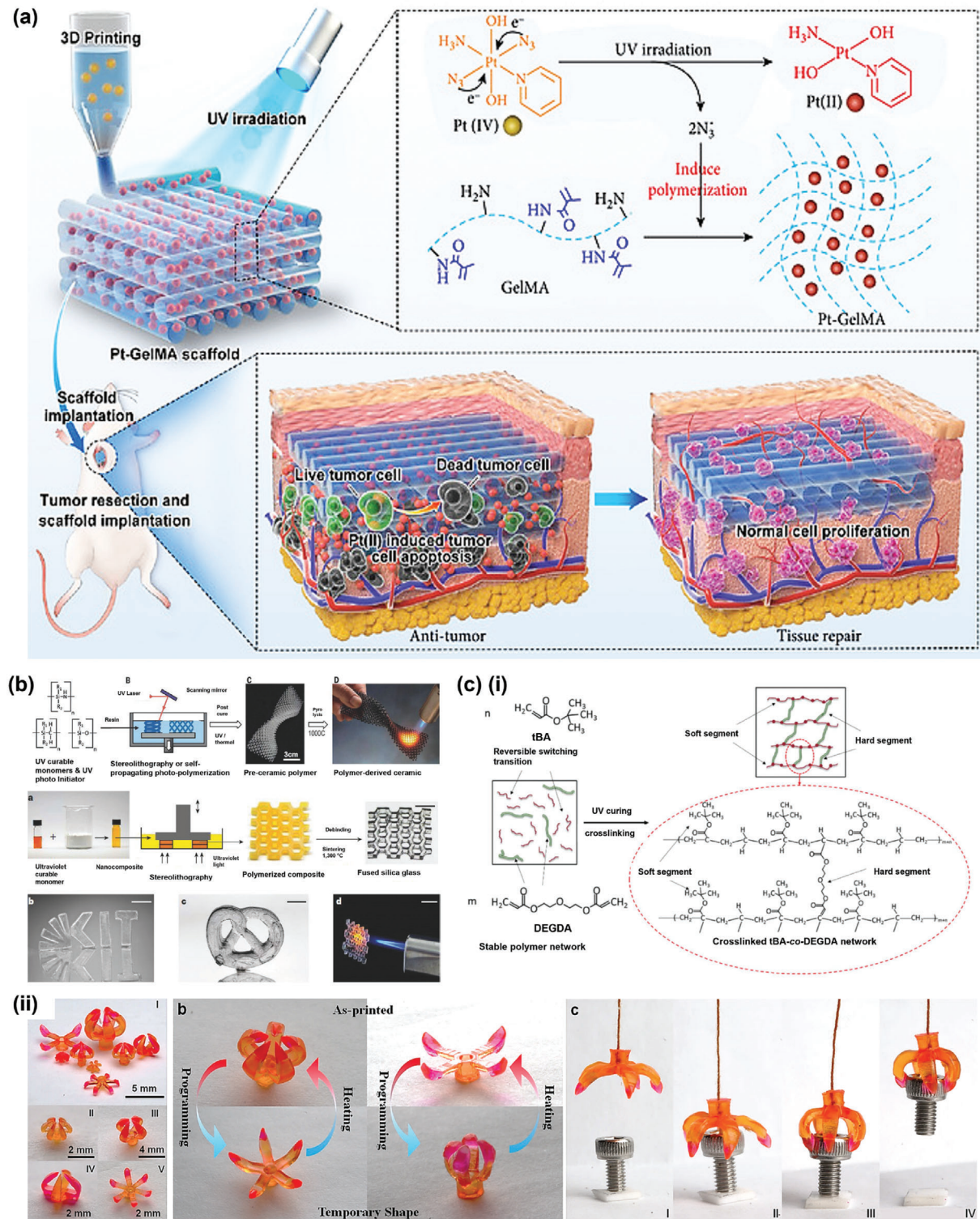


Figure 5. Schematic depiction of the materials used in 3D printing techniques a) 3D-printed GelMA scaffold with Pt (IV) prodrug initiator for tumor treatment, upon irradiation, the Pt (IV) prodrug reduced to Pt (II) and produces N_3^{\bullet} to initiate the polymerization of the GelMA. Following implantation at the tumor site, the Pt-GelMA scaffold effectively kills and prevents the growth and metastases in vivo and serves as a tissue repair platform. Adapted with permission.^[117] Copyright 2022, American Association for the Advancement of Science. b) 3D printing of polymer-derived ceramics and fused silica glass. Adapted with permission.^[118] Copyright, 2018, Wiley. c) (i) structure of a shape memory polymer (tBA-DEGDA) dependent on the networking between UV photopolymerization of tBA monomer and DEGDA crosslinker. Adapted with permission.^[94] Copyright 2018, Royal Society of Chemistry. (ii) fabrication of multi-material gripper with shape memory polymers. Adapted with permission.^[116] Copyright 2016, Nature Portfolio.

Table 3. List combined 3D printing and electrospinning techniques with advantages and potential applications.

Hybrid biofabrication approaches	Materials	Effects and advantages	Application	References
Extrusion-based printing and needle-based electrospinning	Poly(lactide-co-caprolactone)	Development of aligned collagen hydrogel	Peripheral nerve regeneration	[120]
	Polycaprolactone/carbon nanotubes/Gelatin methacryloyl	Reduced cellular damage and early maturation of the cardiomyocytes, manufacturing of complex structures	Cardiac tissue regeneration	[128]
	Poly lactide/polyhedral oligomeric silsesquioxane	High proliferation and differentiation of stem cells, mimicking the native microenvironment of cells	Intervertebral disc regeneration	[129]
Fused deposition modeling and needle-based electrospinning	Poly L-lactic acid/gelatin	Improved cell adhesion, biocompatibility, cellular entrapment, and ease of fabrication method	Subchondral bone and nasal cartilage regeneration	[124e]
Extrusion-based printing and electrospinning	Polycaprolactone/collagen/alginate	Myogenic differentiation, vascularization, and development of cell-laden micro-nanofibers	Muscle tissue engineering	[130]
3D printing utilizing handheld electrospinning	Polylactic acid/gelatin	Improved mechanical strength, degradability, fast production, stability, portability, and economical	Skin tissue regeneration	[131]
3D printing of a sacrificial scaffold and needle-based electrospinning	Poly(glycolic acid)/poly(ethylene glycol)/polyvinyl alcohol	Development of potential scaffold delivering cells to the wound-affected area.	Wound healing	[132]
3D bioprinter and needle-based electrospinning	Polylactic acid/graphene oxide/polyurethane	Highly antibacterial and enhanced cellular infiltration with external support and protection	Tracheal regeneration	[133]
Direct deposition 3D printing and electrospinning	Polycaprolactone and gelatin	Enhanced biocompatibility, proliferation, cell infiltration, and improved printing resolution	Bone tissue engineering	[134]
Electrohydrodynamic jet writing and needle-based electrospinning	Polydimethylsiloxane	Novel fabrication strategy for microdevices with moveable membranes, pillar varieties, and porous scaffolds	Soft robotics and biomedical engineering	[135]

strategy for achieving reversibility. This can be accomplished by manufacturing hybrid devices comprising two or more distinct materials.^[115] As shown in Figure 5c(ii), 3D printing with multiple SMPs enables the fabrication of microgrippers that can grab and release objects with reversible movement.^[116]

4. Strategies for Combination

4.1. 3D Printing onto Electrospun Fibers

Due to its adaptability, 3D printing can be used for various shapes or surfaces.^[119] However, 3D-printing systems have only been applied to tubular or flat electrospun fibers because of the limitations associated with the topology of electrospun products.^[119,120] A specialized SLA-based printer can deposit a photoresponsive hydrogel on top of the aligned electrospun fibers of PCL and PCL–gelatin scaffolds in a flattened form Ref. [121] Additionally, the fused deposition modeling method has been employed to print polylactide-reinforced meshes made

of PCL, collagen, and gelatin derivatives on one surface of the electrospun fibers.^[119] The fused deposition modeling technique has been used to coat electrospun PLLA–heparin tubular scaffolds with an interior diameter of 5 mm by employing an individual PCL loop as the outermost shield of the tube.^[122] The rapid prototyping technique was employed to incorporate a 0°/45° porosity architecture onto the electrospun PCL structures by spinning the mandrel axis carrying the tubes.^[122b,123]

4.2. Electrospinning onto 3D-Printed Structures

Depositing electrospun filaments onto a 3D-printed scaffold is a quick and easy method of accumulating nanofibers on a 3D construct. This straightforward and affordable method has been employed by several researchers. Typically, scaffolds are manufactured using the 3D-printing technique first. A variety of polymers, including PCL, poly(ethylene oxide terephthalate),

poly(lactic acid), polyurethane, PLGA, PLLA, and methacrylic resins, have been used to manufacture 3D constructs.^[124] The most common layout for 3D-printed structures is a flattened shape with networks, whereas the shapes of different constructs can be altered depending on their application.^[124a,125] Rajzer et al.^[124e] fabricated gelatin–PLLA scaffold by combining electrospinning with a 3D-printing system for cartilage and bone regeneration. They developed a hybrid scaffold by forming a top layer of gelatin nanofibers on a fused deposition modeling-printed porous PLLA scaffold. They found that the developed construct could potentially be applied to subchondral and cartilaginous bone regeneration. An electrospun fiber framework and 3D-printed structures created a capsule structure. A 3D printer uses laser-cured liquid resin to generate a structure with a substantial external framework and a small interior lattice to establish a luminal space.^[126] The electrospinning equipment can be positioned before a grounded metallic sheet and wired to an electric current motor using a printed structure filled with NaCl as the collecting unit. Then, the motor can be rotated consistently while manufacturing the capsule to manage the fiber diameter and packing density. Furthermore, electrospinning onto 3D-printed structures can be used to obtain biomimetic fibrous structures for cardiovascular tissue regeneration.^[127] Combining these techniques offers various advantages for creating complex geometrical structures.^[126] Several hybrid techniques involving 3D printing and electrospinning with their applications are given in Table 3.

5. Development of Biomimetic Structures and Tissue-Engineering Applications

Biomimetic structures are of significant interest in tissue-engineering applications. Biomimetic structures refer to the development and design of materials based on the biological entities present in nature. For example, gardeners typically create flowerbeds, and due to the emergence of 3D printing technologies, it is now possible to mimic structures for tissue-engineering applications. For instance, bone is an essential body part that may be regularly repaired to preserve its load-supporting properties.^[136] Nevertheless, bone remodeling capacity is largely compromised by pathological conditions and the size of the defect.^[137] Bone regeneration is a medically intricate process that requires considerable effort to compensate for the strength of bone tissue and involves the interaction of numerous cell types and biological variables.^[138] Large bone deficiencies necessitate surgical intervention using bone grafts to restore damaged tissues. In addition to conventional treatment methods, tissue engineering has been developed as an alternative option for repairing bone abnormalities. This technique creates a dense and structured scaffold that provides structural stability and a 3D regeneration milieu with adaptable bioactivity. The 3D-printing method allows the fabrication of complex geometries that can pinpoint precisely where the cells, biomaterials, and other components are located within the scaffold. At the same time, a fibrous construct is considered a viable substitute that closely resembles the natural microenvironment of the cell. In tissue-engineering applications, mimicking a native environment of the cells is pos-

sible by producing a micro–nanofibrous scaffold with the desired mechanical strength. Hence, in creating biomimetic structures, the fields of 3D printing and electrospinning hold great potential for tissue regeneration as an alternative to regenerative medicines.^[139,140]

5.1. Flowerbed-Inspired Biomimetic Structures

Angiogenesis and osteogenesis must be coupled during bone remodeling.^[141] Typically, biomaterial-mediated vascular development focuses on vascular sprouts infiltrating the implanted 3D construct from the microvasculature of the surrounding tissue. In this context, stimulating the development of a vascular network in bioactive scaffolds is crucial. Inspired by the morphological and functional properties of bone remodeling, a bone microenvironment-imitating framework with a hierarchical architecture and appropriate bioactivity should be conceptualized. In most cases, gardeners create flowerbeds ornamented with flowers and plants encircled by fences. When flowers bloom, they draw a variety of pollinators (including butterflies and bees) that help generate pollen. This specific geometry inspired Zhou et al.,^[142] bearing its biological purposes in mind, to develop a bone microenvironment-imitating scaffold by combining electrospun nanofibers with a 3D-printed framework. The 3D-printed structures served as walls or fences to contain the plants, and the assembled nanofibers laden with bioactive ingredients served as flowers in the center of the flowerbed (Figure 6a(i)). To ensure the desired controlled release of dual factors promoting osteoclastogenesis and angiogenesis, strontium-containing hydroxyapatite (SrHA) and dimethyloxalyglycine-loaded mesoporous silica nanoparticles (DMSNs) were embedded into a 3D-printed PCL microfilament (SrHA-PCL) and electrospun PLGA–gelatin nanofibers (DMSNs-PG). Next, the porous structures of SrHA-PCL were filled with a nanofiber suspension of DMSNs-PG to formulate the biomimetic construct (DMSNs/SrHA-PGP) (Figure 6a(ii)). Further characterization of the scaffold revealed the presence of elements such as Sr, and the water contact angle results showed the enhanced hydrophilicity of the DMSN/SrHA-PGP composite scaffold. The mechanical properties of the scaffolds were significantly enhanced by the addition of SrHA to the PGP composite. Importantly, the compressive modulus and strength of the scaffold containing SrHA fell within the spectrum of the human tubular bone.^[143] Degradation tests revealed that the degradation of the PLGA–gelatin fibers provided adequate space, allowing tissue expansion, whereas the delayed degradation of PCL offered mechanical stability. The in vitro drug release behavior of dimethyloxalyglycine and Sr²⁺ indicated synchronous delivery from the scaffold (Figure 6b). The in vitro proliferation and angiogenic effects of human umbilical vein endothelial cells (HUEVCs) on composite scaffolds were observed using confocal microscopy. The results revealed a drastic increase in the cell number with the culture duration (Figure 6c). Owing to the positive outcomes of the in vitro analysis, an in vivo assessment was performed to study bone regeneration efficacy. Micro-CT evaluation was carried out at 8 and 12 weeks and confirmed the development of new bone at the defect site (Figure 6d). New bone formation was further verified by hematoxylin and eosin and Masson's trichrome

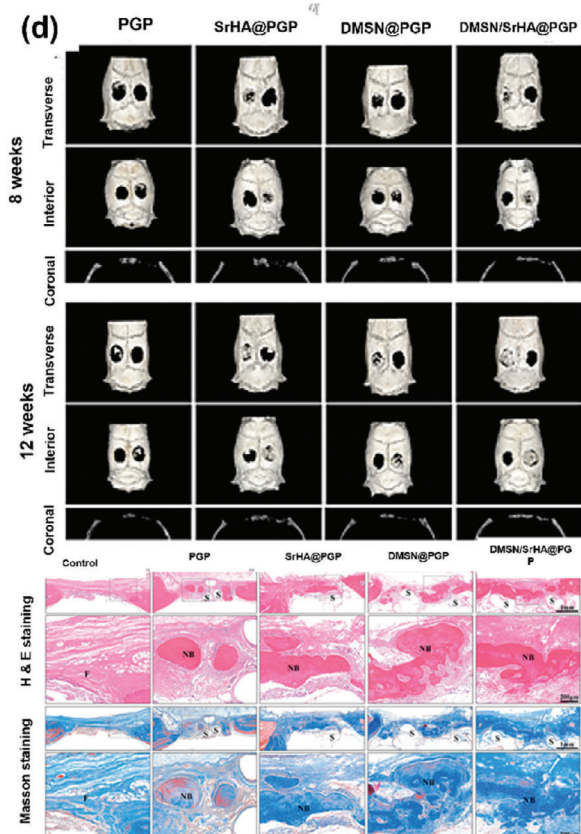
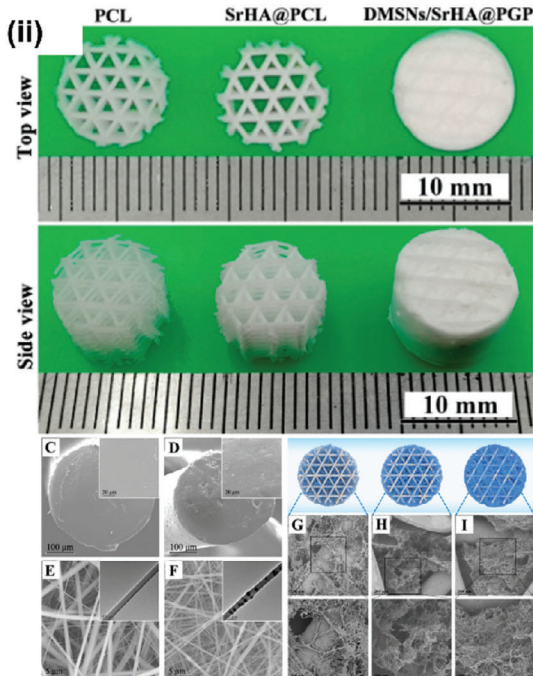
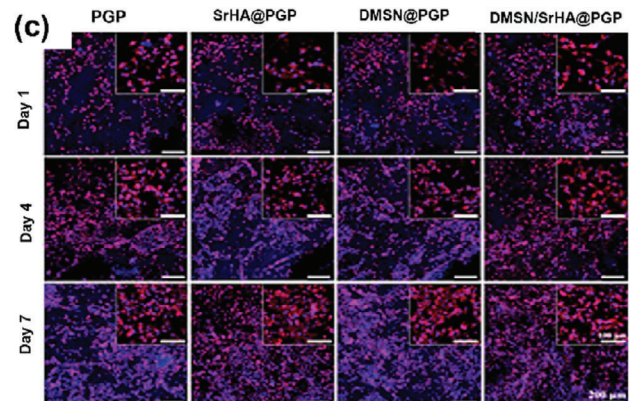
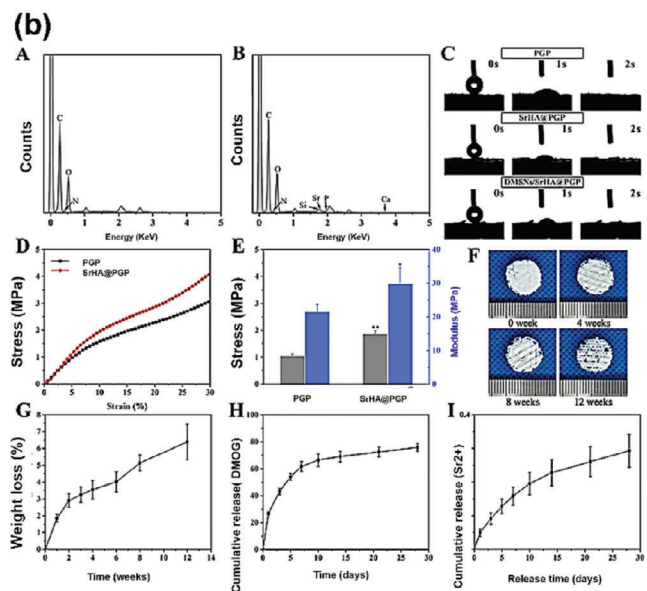
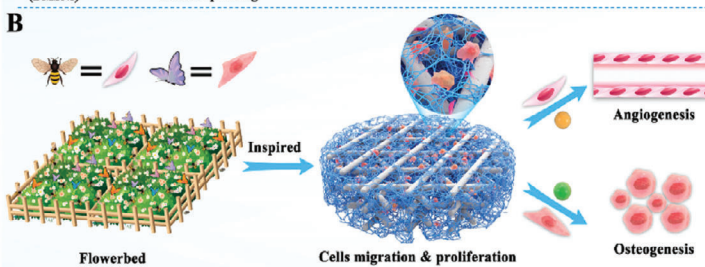
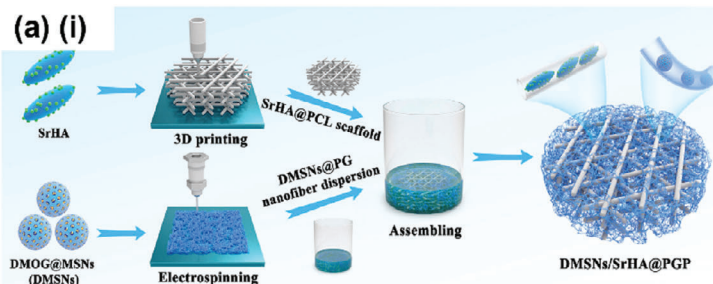


Figure 6. a) (i) The combined fabrication process of the biomimetic flowerbed structure. (ii) Preparation of the construct with different nanofibers content with SEM analysis. b) Chemical characterization of the developed scaffold. c) Cell proliferation rate upon culturing for various time intervals on the scaffold. d) In vivo evaluation of the bone regeneration efficacy of the scaffold. e) H&E and Masson trichrome staining of the rat calvarial bone defect model for histological analysis. Adapted with permission.^[142] Copyright 2023, American Chemical Society.

staining. Histological evaluation confirmed the synergistic potential of SrHA and dimethyloxalyglycine in promoting osteogenesis (Figure 6e). The study concluded that the release of SrHA and dimethyloxalyglycine had a synergistic impact on promoting rapid vascularization by stimulating the immunoregulatory effects and the hypoxia-inducible factor (HIF)-1 α signaling pathway.^[142]

5.2. Development of a Biomimetic Intervertebral Disc

The intervertebral disc is the largest vascular tissue in the body. It comprises three structures: the annulus fibrosus, nucleus pulposus, and vertebral endplates. The annulus fibrosus consists of 15–25 circular films of collagens I and II. The nucleus pulposus is a gel-resembling matrix of collagen, water, and proteoglycan encircled by the annulus fibrosus. The intervertebral disc experiences aging and degenerative alterations earlier than other connective tissue types in the body. Spinal fusion, discectomy, and artificial disc substitution are therapeutic approaches traditionally available for intervertebral disc degeneration. Tragically, these procedures do not contribute to regaining function and are associated with side effects, such as restricted mobility, repeated disc herniation, and surrounding segment degeneration. Techniques involving regenerative medicine and tissue engineering can provide relief from discomfort and functional recovery of degenerated tissues. Manufacturing biomimetic intervertebral discs with the help of 3D printing and electrospinning technology can provide a suitable microenvironment for regenerating damaged tissues. Zhu et al.^[129] constructed a biomimetic artificial intervertebral scaffold by combining electrospinning and 3D printing. To mimic the structure of the native intervertebral disc, polylactide was employed to print the intervertebral framework. The aligned permeable polylactide/octa-armed polyhedral oligomeric silsesquioxane fiber clumps imitated the annulus fibrosus, whereas the gellan gum/polyethylene glycol diacrylate hydrogel loaded with mesenchymal stem cells mimicked the nucleus pulposus architecture. The morphological characterization of the biomimetic intervertebral disc fabricated using 3D printing and electrospinning is shown in Figure 7a. The mechanical characteristics of the scaffolds were evaluated. They exhibited a tensile modulus greater than the threshold of the average human annulus fibers, resembling the requirements for creating a complicated mechanical environment for the intervertebral disc (Figure 7b). The compression modulus of the hydrogel was estimated to be \approx 10 MPa, which provided high mechanical support for tissue repair. The properties of the designed intervertebral disc scaffold were controlled using 3D printing according to the desired characteristics. An *in vivo* study using this approach revealed that the height of the disc enables significant deposition of collagen and proteoglycan required for the nucleus pulposus (Figure 7c). Hence, this study provides a potential approach for biomimicking structures for tissue regeneration and repair.^[129]

5.3. Development of a Biomimetic Vascular Structure

Vascular networks are essential for maintaining the function of the majority of tissues by simultaneously offering cells ad-

equate amounts of nutrients and oxygen and enabling effective metabolite elimination.^[144] Cells typically reach a distance of \approx 150–200 μ m from capillaries within microvascular networks during growth.^[145] Conventional scaffolds often exhibit simple permeable architectures that facilitate mass exchange via free diffusion.^[146] The rate of natural vascular ingrowth is typically only a few tens of micrometers per day. With the emergence of 3D-printing technology, Lei et al.^[147] developed an organized vascular microchannel network for a long-term functional transport system. Using 3D printing, a perfusable microchannel, 3D framework, and permeable porous walls were created to provide a polymeric scaffold with a well-arranged hierarchical architecture that resembled biological vascular networks at various levels. Perfusionable microchannel networks were created by 3D printing, a sacrificial caramel-based template using a fused deposition modeling printer. Their study used caramel as the sacrificial template and PCL as the main biomaterial to develop the microchannel structure. Thermoplastic PCL/polyurethane and thermoset poly(glycerol-sebacate urethane) were used to mimic the native vascular system. Subsequently, the designed hierarchical vascular networks were combined with PCL nanofibers to mimic the natural extracellular microenvironment and facilitate cell proliferation and differentiation.^[63] The developed vasculature system exhibited highly porous and perfusable capabilities, both *in vitro* and *in vivo*.

If further promoted, mass exchange sustains a high density of cardiac cells, contributing to longevity and assisting in the integration of tissue revascularization in epicardial and subcutaneous implantations. The vasculature system effectively reduced fibrosis following myocardial infarction. By integrating 3D printing and electrospinning, Fukunishi et al.^[148] developed a tissue-engineered vascular graft for cardiac tissue engineering using co-electrospinning polyglycolic acid and poly(L-lactide-co- ϵ -caprolactone) scaffolds. A computer-aided mandrel was first designed and printed using a 3D printer, followed by electrospinning of fibers around the mandrel (Figure 7d). Upon implantation into a sheep model, the graft showed high biocompatibility and tissue remodeling. Figure 7e(i) shows hematoxylin and eosin micrographs, indicating successful endothelialization associated with the graft, similar to the native inferior vena cava. Furthermore, collagen deposition, maturation, and patterns confirmed by picrosirius red and Masson's trichrome staining showed similar patterns in tissue-engineered vascular grafts and the native inferior vena cava (Figure 7e(ii)). The results of their study indicated successful tissue remodeling and CD68 $^{+}$ macrophages triggered an inflammatory response in the enhanced wall thickening of the graft, with an efficacy resembling that of the native inferior vena cava, suggesting a promising approach for vascular tissue engineering.^[148]

5.4. Skin Regeneration

Skin is the first line of defense against harmful substances and is essential for maintaining homeostasis.^[149] It is prone to injury, as it is the outermost organ of the body. The structure and function of the epidermis must be restored as quickly as possible after trauma. Nevertheless, none of the current skin substitutes, including epidermal and dermal substitutes, can

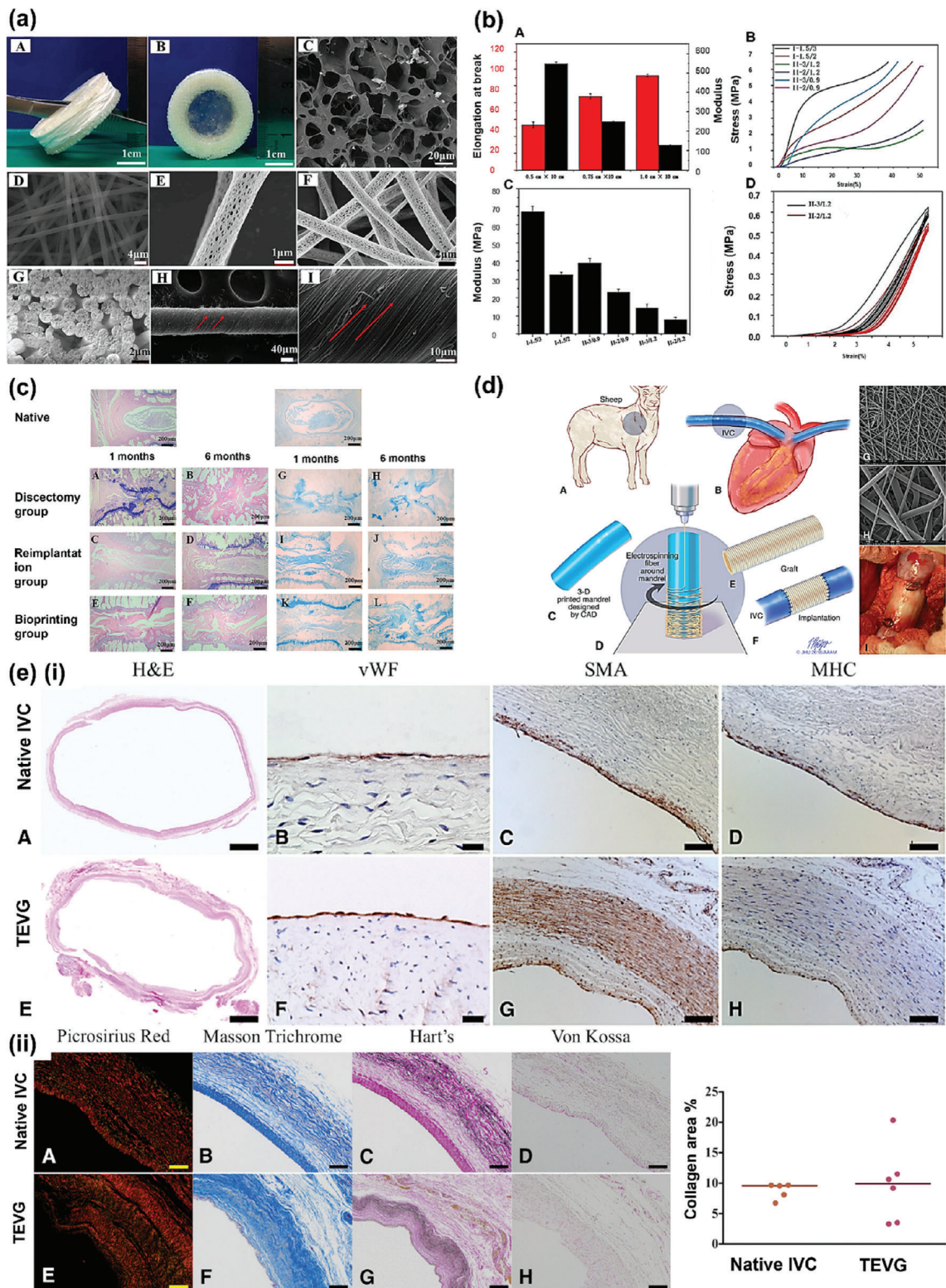


Figure 7. a) Development and characterization of the 3D-printed intervertebral disc. And b) its mechanical properties. c) Histological evaluation of the scaffold with H&E and Alcian blue staining. Adapted with permission.^[129] Copyright 2021, Elsevier. d) Schematic illustration of the vascular graft developed with combined technologies. e) (i) Hematoxylin and eosin, (ii) picrosirius red and Masson's trichrome staining photomicrograph of vascular nano tissue formation of the designed structure with the collagen and elastin accumulation in the tissue-engineered construct. Adapted with permission.^[148] Copyright 2017, Elsevier.

entirely replicate or reestablish all the features and capabilities of natural skin.^[150] Modern biomanufacturing methods, including 3D printing and electrospinning, have been combined with bioactive chemicals, cells, and biomaterials to exploit novel enhanced skin structures.^[151] By employing solvent exchange deposition modeling, a versatile PLGA scaffold was manufactured using a quick *in situ* manufacturing approach, which was then coupled with electrospun nanofibers to create skin substitutes.^[152] In a rat model study involving *in vivo* wound repair and histological evaluation, the use of a scaffold-anchored 3,4-dihydroxyphenethylamine–epidermal growth factor, applied through a bio-orthogonal technique, effectively enhanced full-thickness wound healing.^[153] Miguel et al.^[154] initially described the development of a 3D dermis asymmetric structure using electrospinning and 3D-bioprinting methods.^[154] The top electrospun layer provided a suitable atmosphere for the penetration of cells and the exchange of nutrients with dense and interconnected nanofibrous networks. The bottom layer, comprising the 3D-printed structure with suitable porosity, wettability, and biological characteristics, allowed for cell migration, adhesion, and proliferation, preventing the emergence of *Staphylococcus aureus* and *Pseudomonas aeruginosa*.^[154]

One of the most agonizing complaints of patients is discomfort from both acute and chronic wounds.^[155] It has been demonstrated that patients have the greatest difficulty in replacing dressings. Recently, researchers have concentrated on analgesics and appropriate dressing materials to reduce patient discomfort while changing wound dressings. Maver et al. incorporated analgesic drugs, including diclofenac sodium and lidocaine, into combined electrospun fibers and a 3D-printed scaffold^[125] to create a single dressing. In this dressing system, the drug contained in the electrospun fiber was instantly activated upon contact with the injury, providing immediate pain relief. After an extended period, the drug-loaded scaffold began to work and permanently reduced pain. To accelerate wound healing, a resorbable fibrous wound dressing that can deliver a cellular payload was developed based on a sacrificial 3D-printed structure.^[132] To achieve this, an electrospun composite with an inner reservoir was produced using 3D-printed sacrificial components. The confined empty space created by removing the sacrificial structures generated space for cells and other payloads to be incorporated. The fibrous layer of the electrospun fibers provided a large surface area, allowing the cells to attach. The results showed that the construct improved neovascularization, which aided wound healing.

5.5. Development of a Biomimetic ECM

The ECM structure, characterized by its inhomogeneity and complexity, has been extensively studied in several tissues, including the fibrocartilage, bone, ligament, and the Achilles tendon. Despite enormous variations among tissues, the composition and architecture of the ECM are crucial for maintaining physiological equilibrium and the development of pathologic conditions.^[156] The dura mater is a connective tissue barrier surrounding the spinal cord and is an intricate microstructure with several physiological roles. It is frequently damaged following spine surgeries, leading to epidural fibrosis and several complications. Collagen fibers in the dura mater are oriented parallel to the longitudi-

nal orientation, with a few haphazardly dispersed fibers entwining with one another to form a complex heterogeneous structure that exhibits different characteristics on various sides.^[157] In dura mater destructions, fibroblasts perform a complicated role in the establishment of fibrosis and repair, presenting a difficult obstacle for conventional homogenous scaffolds in regulating cellular processes. The two major conditions that must be effectively prevented to substantially repair impaired dura tissue are neurological dysfunctions and arachnoiditis induced by fibrosis. This fibrosis results from an excess of ECM constituents, primarily fibronectin and collagen accumulation in the laminectomy space, due to the tireless proliferation and activation of myofibroblasts. Influenced by its functionality, microstructure, and tissue fibrosis development mechanism, Xu et al.^[158] hypothesized that a customized homogenous scaffold could meet the demands of dura mater regeneration by controlling various cell activities.^[158] Encouraged by the heterogeneous morphology of the dura mater, they fabricated a double-layered diverse micro–nanofiber framework, with an internal anisotropic surface maintaining inactive fibroblast characteristics and an outer dense surface inhibiting myofibroblast attachment, aiming to simultaneously resemble the dual properties of the dura mater to aid healing and avoid fibrosis. Figure 8a shows a schematic depiction of the heterogeneous micro–nanofibers regulating cell properties to heal dura meta defects and prevent fibrosis. A heterogeneous dual-layer fibrous scaffold was prepared using collagen I and SF with varying collection durations (30, 60, 120, and 120 s, and 1 and 2 h) and different mixing ratios of collagen I to SF (5:95, 10:90, 15:85, 20:80, 25:75, and 50:50). Different topologies were constructed by controlling the experimental conditions, including random and anisotropic topologies (Figure 8b). Integrins mediate cell adhesion to the ECM and play key roles in controlling cellular processes. To assess the effects of the chemical composition and topology of the fibers, fibroblasts were cultured on a fibrous matrix to detect integrin activation. Following 12 h of culture, the flow cytometry and immunofluorescent staining images revealed an increased expression of integrin- β 1 with a well-spread structure of fibroblasts in random SF-collagen I fibers (RSCF), with an elongated morphology of the fibroblasts observed in the aligned SF-collagen I fibers (ASCF) along with reduced integrin β 1 expression. The flow cytometry results of this study revealed that an elevated collagen concentration led to an increase in integrin β 1 expression in both increased and random fibers. Nevertheless, integrin activation on random fibers was more efficient than that on the anisotropic matrix (Figure 8c) at the same collagen I mixing ratios. This study established that the anisotropic structure suppressed integrin β 1 activation and an enhanced concentration of collagen I promoted integrin β 1 activation by increasing the adhesion density. Focal adhesion reorganization by vinculin expression was further investigated using topology-guided variations. Immunofluorescence was used to examine vinculin expression in both random and anisotropic matrices. Vinculin on RSCF fibers was expressed at the edge of the fibroblasts with a thick and punctate morphology red fluorescence, which was absent in the anisotropic fibers, revealing alterations in the adhesion phases of cells in different topological structures. The proliferation, spreading, and morphology of the cells were further characterized using scanning electron microscopy after 48 h of

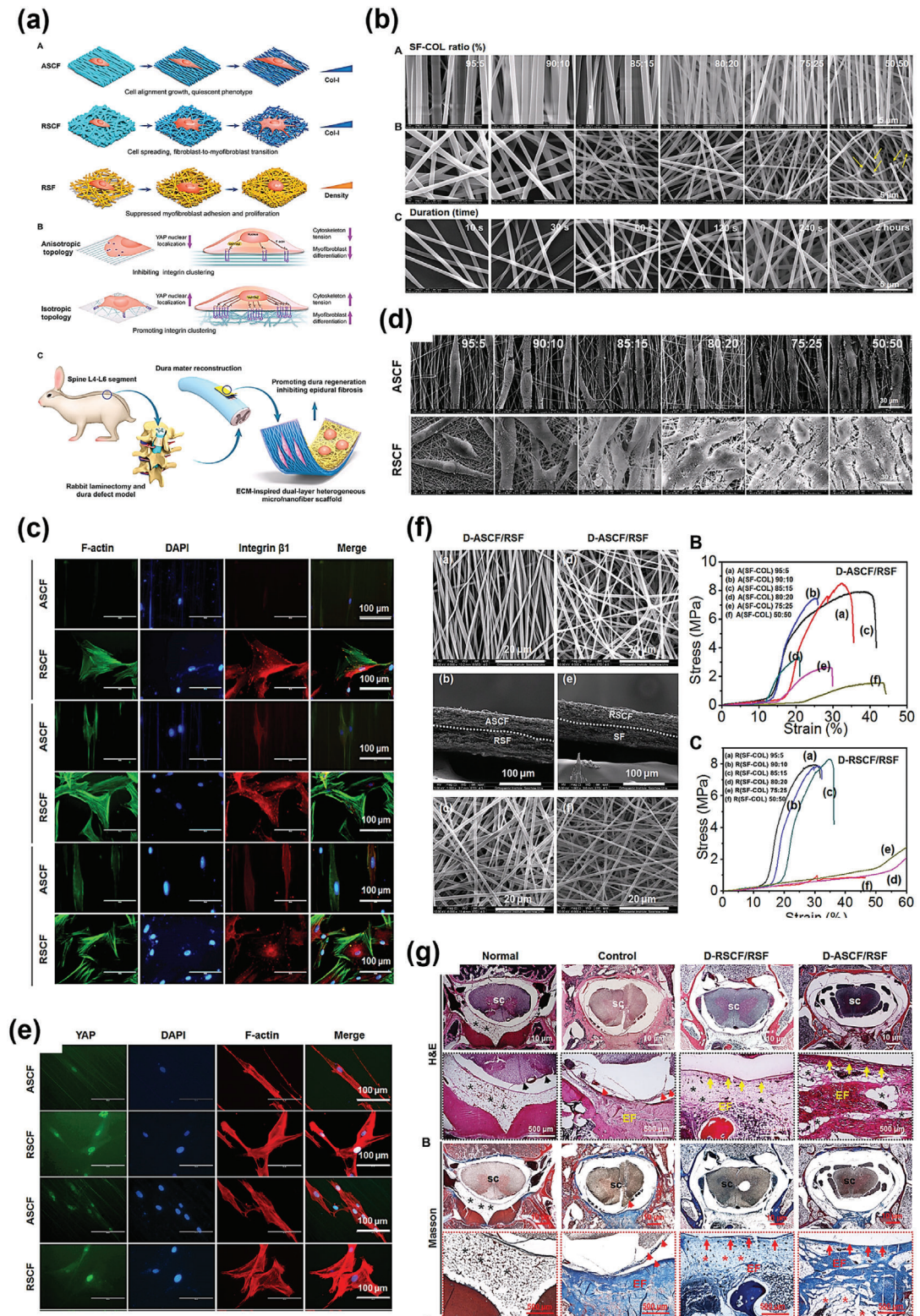


Figure 8. a) Diagrammatic representation of the heterogeneous fibrous structure controlling various cellular responses to heal the dura damage and avoid epidural fibrosis. b) Characterization of ASCF and RSCF fibers with different Col-I and SF ratios. c) Evaluation of heterogenous nanofibers on the expression of integrin protein. d) Morphological characterization of fibroblasts and myofibroblasts cultured on micro-nano fibers. e) Anisotropy regulated function and YAP activity of fibroblast cells on heterogeneous fibers. f) Physical characteristics and biological evaluation of the double-layered heterogeneous fibrous scaffold. g) In vivo, evaluation of the epidural tissue and spinal dura mater following 8 weeks of implantation. Adapted with permission.^[158] Copyright 2020, Science.

culture. This indicated that the cells on ASCF exhibited a spindle morphology with polarization and elongation owing to the contact supervision of the topology and anisotropic fibers. However, the cells grown on random fibers were scattered in different orientations, forming sizable lamellipodia (Figure 8d). The increased concentration of collagen I suggested an increase in the cell density and scattering area. The activation of quiescent fibroblasts during tissue repair is represented by the emergence of α -SMA tension fibers associated with the F-actin cytoskeleton. Immunofluorescence staining and the percentage of α -SMA activation were manually calculated for each group. The study revealed that an anisotropic matrix reduced α -SMA expression and inhibited the differentiation of fibroblasts into myoblasts. Collagen I expression from cells cultured on ASCF and RSCF showed that collagen I generated from fibroblasts on ASCF exhibited a directed distribution and that the fibroblasts on RSCF were disorganized, suggesting a topology-guided role of matrix fibers in ECM secretion and remodeling. Localization of yes-associated protein (YAP) in the ASCF and RSCF enhanced activation more in random fibers than in anisotropic fibers. The cells cultured on random fibers exhibited an expanded cytoskeleton, with increased YAP expression in the nucleus (Figure 8e). In contrast, the cells grown on the anisotropic matrix showed a small expanding area, with several YAP-associated cells. The collagen fibers constituting the dura mater are arranged in a diverse array: the longitudinal collagen fibers remain parallel, whereas the fibrous fibers are haphazardly interwoven with each other. Based on this heterogeneous structure, a dual-layered heterogeneous construct was fabricated to mimic the native structure of the dura mater, promoting the healing of the spinal dura and inhibiting scar formation. A dual-layered heterogeneous scaffold was prepared by combining the internal layer with ASCF or RSCF and an external layer made of SF. Scanning electron microscopy images of the fabricated scaffold revealed an aligned and compact structure in the internal layer, with irregular interwoven fibers and higher porosity on the surface of the internal layer. Mechanical characterization of the scaffold suggested that the internal layer using 15% collagen I and the outer layer electrospun at 3 h exhibited remarkable mechanical properties (Figure 8f). The biological properties of the dual-layered scaffold showed that the cells on the internal anisotropic layer extended and elongated along the fibers, and the cells on the internal layer with random fibers exhibited a well-spread and flat structure with lamellipodium development. Moreover, the fibroblast cells on the scaffold exhibited infiltration into the internal layer of the layered scaffold, despite the irregular or anisotropic architecture. In contrast, myofibroblasts could grow in the outer (SF) layer, showing the barrier properties of the external layer upon infiltration. To compare the *in vitro* results, an *in vivo* analysis covered the defective spinal dura with a dual-layered scaffold (D-RSCF/RSF or D-ASCF/RSF). Epidural tissue attachment among the controls (without scaffold) showed increased scar adhesion between the defective dura and surrounding tissue, which was significantly lower in the treatment groups (D-RSCF/RSF and D-ASCF/RSF). Furthermore, hematoxylin and eosin and Masson's trichrome staining revealed no new dural tissue development in the control group (Figure 8g). In contrast, the group treated with the D-ASCF/RSF scaffold showed the formation of continuous collagen at the defective site, mimicking native tissue. In contrast,

a new, discontinuous, and irregular collagen layer resembling scar fibrosis was observed in the D-RSCF/RSF group. Nevertheless, both D-ASCF/RSF and D-RSCF/RSF showed the potential to prevent epidural scar development. Next, an immunohistochemical study of collagen I and α -SMA in epidural tissue was conducted to study the influence of a double-layered scaffold in inhibiting scar adhesion. The control group exhibited dense collagen I type, whereas D-ASCF-RSF and RSCF/RSF exhibited reduced collagen I type expression, resembling native epidural tissue. Additionally, the control group showed higher α -SMA-positive cells culturing near the blood vessel and the corner of the wound. In contrast, the ratio of α -SMA-expressing fibroblasts significantly decreased in the D-ASCF/RSF and D-RSCF/RSF treatment groups. Consequently, *in vivo* analysis further revealed that the inner anisotropic structure of the double-layered scaffold promoted healing and regeneration of the dura tissues. The outer layer of the SF fibers inhibited myofibroblast proliferation and adhesion at the laminectomy site. It also decreased the α -SMA-expressing fibroblasts to avoid excessive ECM constituent deposition and to prevent fibrosis and scar formation in epidural tissue.

5.6. Development of a Biomimetic Leaf-Venation Structure

The ability to successfully construct functioning cardiac tissues offers considerable potential for cardiotoxicity testing, disease modeling, and repair of the impaired myocardium in countless patients. The heart is an intricate, effective pump with crucial anatomical and functional features. The extremely aligned and closely packed cardiac cells create intercellular interactions that communicate the contractile force and electromechanical behavior of the myocardium, which effectively transports a substantial amount of nutrients and oxygen to meet the metabolic needs of the myocardium. The simulated anisotropic characteristics of the myocardium display various effective rigidities in the circumferential orientation to nourish the systole and diastole of the heart. Over the past few decades, a significant amount of research has been conducted to develop cardiac structures that mimic the extracellular microenvironment, which possesses multifunctionalities that imitate cardiac tissue features and correlate with the biological function and structural organization of the natural myocardium.^[159]

Previously, several artificial scaffolds with precisely aligned electrospun fibers were created to mimic anisotropic architecture, offering topographical signals to guide cell arrangement. However, these scaffolds were devoid of ECM signals necessary for cell integration and hierarchical angiogenesis. To tackle these shortcomings, Mao et al.^[160] developed a leaf-venation-directed technique abbreviated as "LVD" for generating a functional prevascularized scaffold mimicking the electrophysiological and anisotropic properties of the myocardium. Leaf venation is a nature-designed, hierarchically organized network composed of aligned fibers and closely spaced cells that mimic electrophysiological functions in the myocardium. In addition, leaf venation has a highly effective fluid flow function.^[161] Influenced by these features, a leaf venation system was employed to govern the anisotropy of hydrogel-cell hybrids into tissue structures with a compact layout and robust functions. The LVD

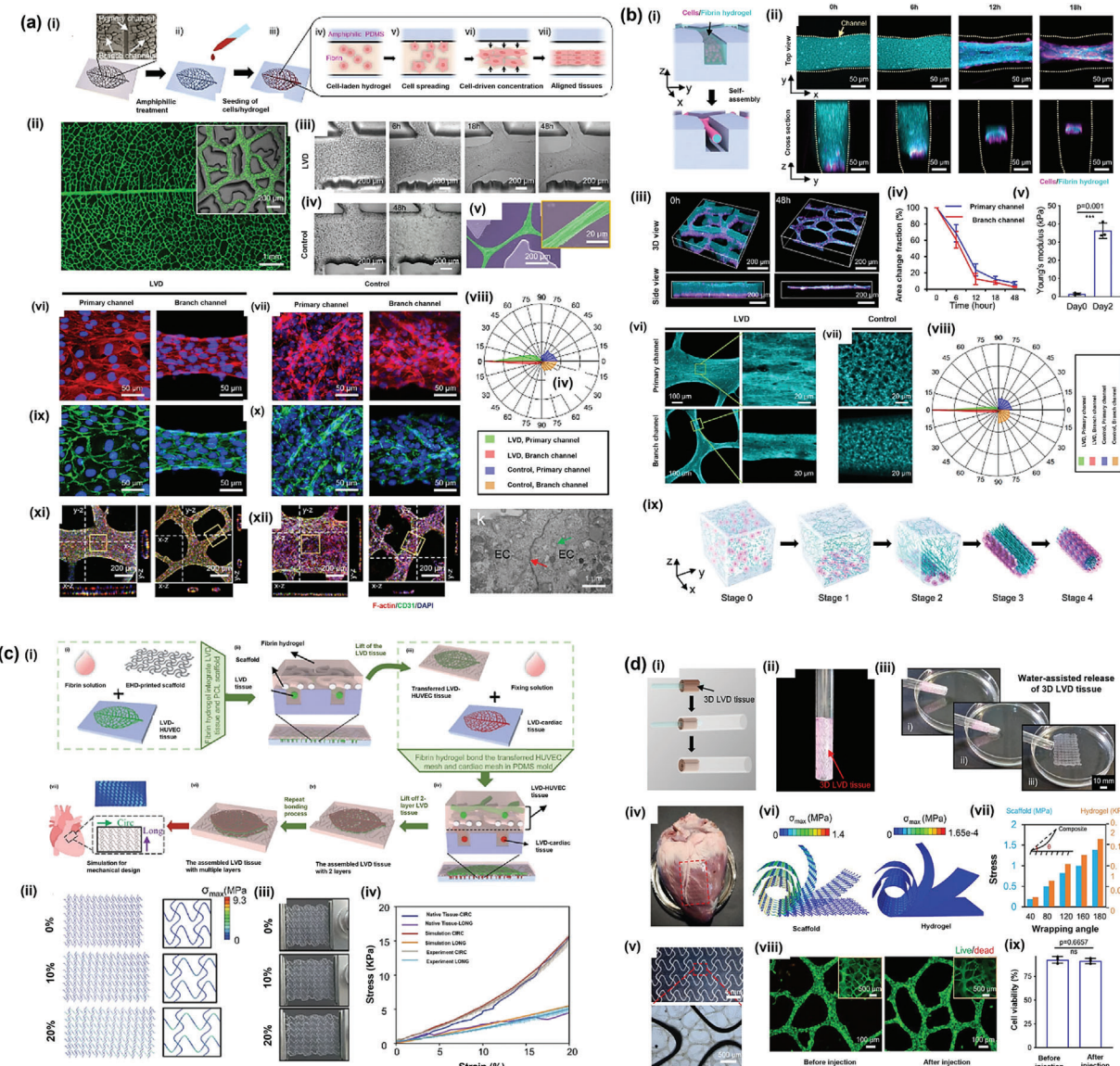


Figure 9. a) (i–xiii) Schematic illustration of the LVD technique for fabricating large-scale tissues with tight intercellular connections and highly synchronized populations using HUVECs. b) (i–ix) Investigation of the development mechanism of LVD-HUVEC tissues with densely packed tubular features and structural evaluation of the engineered LVD-rat cardiac tissues. c) (i–iv) Development of 3D pre-vascularized LVD cardiac tissue construct with tunable mechanical characteristics. d) (i–ix) Injectable administration of the 3D LVD-cardiac tissue construct. Adapted with permission.^[160] Copyright 2023, Nature Portfolio.

method utilizes microchannels resulting from the leaf-venation system as a pattern of confinement to direct the morphological development of highly populated cells in the hydrogel. A polydimethylsiloxane surface with microchannels, including a main channel and several branched channels, was produced using a leaf-venation system framework.^[162] Amphibolic production was conducted to avoid adhesion between the cell-hydrogel and PDMS and was considered the treatment group, whereas the non-amphiphilic group was the control group. The microchannels were then gelled by incorporating a cell-loaded fibrin hydrogel solution (Figure 9a(i)). The evenly distributed cells start spreading and applying friction to the matrix to initiate LVD structural features, which allow the contraction of the hydrogel.

gel and self-assembly into tightly packed tissue, eventually resulting in interconnected bundles of tissue aligned within the microchannels.^[163] Figure 9a(ii) demonstrates the LVD technique for successfully designing a large number of prevascular tissues possessing interlinked hierarchical connections restricted to leaf-vein-motivated microchannels. The mixture of hydrogel solution and HUVECs separated from the channels and progressively condensed within the microchannels. After 48 h of culturing, the cells in the treatment group became stable and self-assembled with smooth borders. The cells in the control group remained intact and randomly distributed (Figure 9a(iii,iv)). The scanning electron microscopy images revealed a highly compacted and elongated pattern of the cell

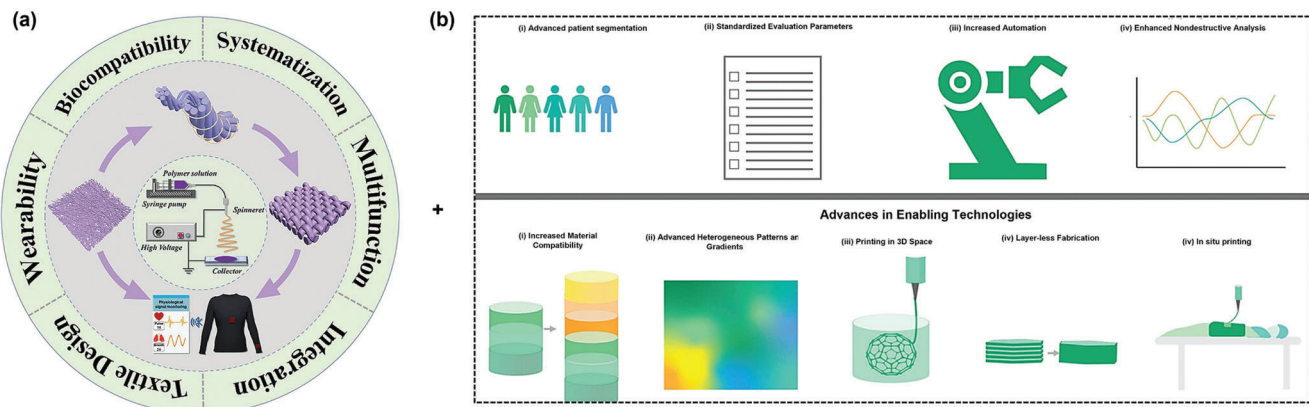


Figure 10. Future research and development of a) Piezoelectric-based nanofibers. Adapted with permission.^[164] Copyright 2023, Wiley b) 3D printing techniques for precise medicine and healthcare. Adapted with permission.^[165] Copyright 2020, Wiley.

bundles (Figure 9a(v)). Characterization of the protein expression and cytoskeleton arrangement of endothelial cells in the LVD system revealed that the cells attained confluence with significant alignment along the microchannels (Figure 9a(vi–viii)). The cells in the control group were randomly arranged in an irregular pattern (Figure 9a(vii,viii)). The cells exhibiting cell-cell contact in LVD-HUVEC tissues exhibited increased expression of the CD31 marker, indicating the phenotypic maintenance of endothelial cells and generation of dense intercellular junctions (Figure 9a(ix–xi)). In contrast, the control group expressed reduced levels of CD31 in a random pattern (Figure 9a(x)). Furthermore, the cells in the LVD structure formed interlinked tubular patterns in all primary and branched channels, while the cells in the control were allocated at the base of the microchannels (Figure 9a(xii,xiii)), revealing the potential for generating a vasculature system *in vivo*. The process of self-assembly of the LVD-HUVECs from an even distribution to a densely arranged aligned tubular structure was further studied (Figure 9b(i)). Figure 9b(ii) shows confocal microscopy images of the cells and fibrin hydrogel cultured over different time intervals. HUVECs settled at the bottom of the fibrin hydrogel after being seeded within the microchannels. Following a 6-h culture, a decrease in fibrin hydrogel thickness was observed, resulting in an enormous reduction in the direction of thickness. Several cells began to line the outer surface of the compressed fibrin rod, but most of the cells remained at the bottom of the hydrogel. After 18 h, the cells migrated from the bottom to the top surface, generating a tubular vascular structure with densely loaded fibrin. Eventually, the haphazardly arranged cells and fibrin formed continuous tubular networks surrounded by cellular membranes. The quantitative outcomes showed that as the growth of LVD tissues progressed, the mean cross-sectional area of the cell–fibrin hydrogel decreased by \approx 13- and 33-fold in the primary and branched channels, respectively (Figure 9b(iii,iv)). A significant reduction in the volume of the cell–fibrin composites resulted in enhanced mechanical characteristics. Hence, following 48 h of culture, the atomic force microscopy results revealed an increase of \approx 45-fold in the average Young's modulus from \approx 0.8 to 37.3 kPa. Densely organized fibrin filaments in the LVD tissue were directed along the microchannels. The fibrin filaments in the control group persisted in a porous structure with a random distribution.

Quantitative data showed that the alignment of fibrin filaments in the control and LVD tissues followed a cellular alignment trend (Figure 9b(v–vii)). The LVD-HUVECs were then encased in a gelatin gel and diffused in a nanobead solution. The results revealed a self-assembly process involving various sequential stages (Figure 9b(viii,ix)). At stage 0, the cell–hydrogel solution was evenly loaded into the microchannels. In stage 1, round cells were located at the bottom of the hydrogel. In stage 2, the cells expanded by exerting a force on the surrounding cells and ECM to gather them in the central area, at which point a strain was generated in the hydrogel along the longitudinal axis of the microchannels. Stage 3 included the combined function of longitudinal strain and cellular force, compressing the hydrogel fibers into a rod-shaped structure. The cells then migrated from the bottom to the surface of the compressed fibers. After reaching the final stage 4, the fibers were more compressed, and the cells attained confluence around the dense fibers and were aligned along the longitudinal axis.

The LVD technique has been further employed to engineer cardiac tissues with aligned, densely packed, and interconnected structures possessing electrophysical properties and beating functions. Furthermore, to avoid the occurrence of post-infarction left ventricular remodeling and ensure the long-term viability of the heart, it is essential to engineer 3D cardiac tissue with appropriate mechanical characteristics and prevasculature. A scaffold-directed technique was developed to allow the transfer and assembly of LVD-HUVECs and LVD-cardiac tissues into 3D tissue composites. An elastic structure with a precisely specified serpentine microstructure was anticipated to replicate the viscoelastic and anisotropic characteristics of the natural myocardium. Figure 9c(i) depicts the assembly and transfer processes of numerous LVD tissues. Figure 9c(ii,iii) shows the finite element analysis simulation and macroscopic images of the 3D construct upon stretching. Figure 9c(iv) depicts a significant consistency in the mechanical properties along the circumferential and long axes, demonstrating the combination of hypothetical and printed structures exhibiting properties similar to those of native cardiac tissues. To prevent chest surgery, implantation of the LVD cardiac structure using minimally invasive techniques was continued to investigate the viability of the construct. The four membrane cardiac constructs were expected to be

administered by tube penetration through the chest wall. Before the injection, the cardiac construct was coiled over a rod and transferred into a tube to stabilize the tissues (Figure 9d(i,ii)). The construct rushed out of the tube in running water and attained its original shape (Figure 9d(iii)). This solution was injected into the ventricle of the ex vivo heart. The construct showed highly adhesive properties upon injection and maintained structural integrity (Figure 9d(iv,v)). Finite element analysis was used to examine the stress-strain distribution in the LVD tissues consisting of the fibrin hydrogel and the scaffold, which revealed an enhanced strain force in the scaffold compared to the hydrogel. The live-dead evaluation showed no remarkable change in the number of viable cells before and after injection, indicating that the compressive stress caused by coiling and fluid-assisted recovery had no detrimental effects on the 3D LVD tissues (Figure 9d(vi-ix)).

6. Conclusion and Future Perspective

Achieving the repair and regeneration of damaged tissues in the field of tissue engineering remains exceptionally challenging. It involves the precise design of a 3D construct that supports the re-growth of defective tissues by incorporating biomimetic mechanical features, an adequate support system, and desirable permeability to facilitate tissue colonization and infiltration with high biocompatibility. Owing to their adaptability in generating structures that range from the micro- to macroscale and by implementing their benefits, such as cost-effectiveness and relative inexpensiveness, 3D-printing techniques have garnered enormous research attention, particularly in recent years. These advantages have made them competitive with conventional production methods, such as machining. 3D-printed scaffolds are used as biomaterials in bioprinting to encapsulate and print cells. However, scaffolds frequently suffer from inadequate structural integrity, despite offering a conducive environment for cells to thrive during construction. To overcome this limitation, hybrid technologies, including electrospinning, must be combined with conventional 3D-printing methods to fabricate cellular microenvironments. Integrating 3D printing and electrospinning substantially affects scaffold manufacturing, overcoming the drawbacks of scaffolds made solely by using 3D printing or electrospinning. This review examined the current status of this hybrid technique in the field of tissue engineering.

Structures mimicking native tissue architecture with a variety of designs, characteristics, and functions have been created by merging the two techniques in diverse ways. These structures have been demonstrated for use in a wide range of biomedical applications, including bones, abdominal tissues, vasculature, and wound healing. The main advantages of the combined methods discussed in this review are as follows: i) the production of a hierarchical structure that mimics the native ECM, facilitating nutrient transport through a 3D printed structure, and ii) the maintenance of long-term structural support by combining the rapidly degrading fibers with delayed degrading 3D constructs, or vice versa. However, the combined approach poses several challenges, such as i) a complicated fabrication process, which requires additional efforts to optimize the desired properties, and ii) a time-consuming process owing to the involvement of more than one technique—the integration of these methods extends the overall time compared to using a single technique.

Future studies should thoroughly examine the performance of hybrid frameworks, including how macroscale processes, such as osmosis, diffusion, and perfusion, influence cell penetration and shape. Additionally, the mechanical characteristics of the scaffolds should be adaptable to the *in vivo* microenvironment, which can be accomplished by combining electrospinning and 3D-printing techniques in multiple ways. The precise morphological characteristics of native tissues can be generated *in vitro* using hybrid technology. The development of polymers required to fabricate structures with various geometries can be achieved using elastomeric polymers to regulate the relationship between structure and properties. The balance among structural support, tissue development, and polymeric deterioration must be adjusted to correct defects of various sizes, reduce tissue overgrowth, and avoid (re)stenosis.

Developing and integrating electrospinning based on piezoelectric materials with 3D-printing technologies can provide an advanced platform for next-generation healthcare management (Figure 10). However, challenges such as multifunctionality, prolonged operation, and cost-effectiveness of the developed structures must be overcome with the emergence of technologies for use in tissue engineering and medicine. In addition, there are numerous potential uses for scalable fabrication methods that combine 3D printing and electrospinning in the areas of *in vitro* assays, immunoassays, drug-testing platforms, biomedical microdevice technology, and customization of the structure and function of tissue engineering scaffolds. Subsequently, the structures developed by combined technology have been tested in pre-clinical and clinical trial phases owing to limitations, such as the inability to tune mechanical efficiency and the discrepancy between polymer breakdown and tissue ingrowth and inflammation. Nevertheless, current studies have revealed that combined technologies significantly surpass individual technologies; hence, these practices should be implemented in routine clinical applications with enhanced features in the near future.

Acknowledgements

This research was supported by the Basic Research Program through the National Research Foundation of Korea (NRF), which is financed by the Ministry of Education (NRF-2018R1A16A1A03025582, NRF-2019R1D1A3A03103828, and NRF-2022R1I1A3063302).

Conflict of Interest

The authors declare no conflict of interest.

Keywords

3D printing, biomimetic structures, combined technique, electrospinning, tissue engineering

Received: October 13, 2023

Revised: January 11, 2024

Published online:

[1] X. Zhang, D. Williams, in *Definitions of Biomaterials for the Twenty-First Century*, Elsevier, Amsterdam, Netherlands **2019**.

[2] U. Jammalamadaka, K. Tappa, *J. Funct. Biomater.* **2018**, *9*, 22.

[3] a) A. Etxabide, T. Garrido, J. Uranga, P. Guerrero, K. de la Caba, *Int. J. Biol. Macromol.* **2018**, *120*, 2094; b) A. Camposeo, L. Persano, M. Farsari, D. Pisignano, *Adv. Opt. Mater.* **2019**, *7*, 1800419.

[4] a) S. Derakhshanfar, R. Mbeleck, K. Xu, X. Zhang, W. Zhong, M. Xing, *Bioactive Mater.* **2018**, *3*, 144; b) L. Lin, Y. Fang, Y. Liao, G. Chen, C. Gao, P. Zhu, *Adv. Eng. Mater.* **2019**, *21*, 1801013; c) F. P. Melchels, J. Feijen, D. W. Grijpma, *Biomaterials* **2010**, *31*, 6121.

[5] P. D. Dalton, C. Vaquette, B. L. Farrugia, T. R. Dargaville, T. D. Brown, D. W. Hutmacher, *Biomater. Sci.* **2013**, *1*, 171.

[6] X. Yang, J. Wang, H. Guo, L. Liu, W. Xu, G. Duan, *e-Polymers* **2020**, *20*, 682.

[7] a) M. M. Stevens, J. H. George, *Science* **2005**, *310*, 1135; b) M. Mohammadi, S. A. M. Shaegh, M. Alibolandi, M. H. Ebrahimzadeh, A. Tamayol, M. R. Jaafari, M. Ramezani, *J. Control Release* **2018**, *274*, 35.

[8] a) F. Zhou, X. Jia, Y. Yang, Q. Yang, C. Gao, S. Hu, Y. Zhao, Y. Fan, X. Yuan, *Acta Biomater.* **2016**, *43*, 303; b) X. Li, Z. Chen, H. Zhang, Y. Zhuang, H. Shen, Y. Chen, Y. Zhao, B. Chen, Z. Xiao, J. Dai, *Polymers* **2019**, *11*, 341; c) D. L. Yang, F. Faraz, J. X. Wang, N. Radacsi, *Adv. Mater. Technol.* **2022**, *7*, 2101309.

[9] X. Lu, C. Wang, Y. Wei, *Small* **2009**, *5*, 2349.

[10] M. M. Kareem, K. Tanner, *Proc. Inst. Mech. Eng., Part H: J. Eng. Med.* **2022**, *236*, 483.

[11] a) L. Wang, A. Ryan, in *Electrospinning for Tissue Regeneration*, Elsevier, Amsterdam, Netherlands **2011**; b) G. R. Mitchell, *Electrospinning: Principles, Practice and Possibilities*, Royal Society of Chemistry, London, UK **2015**.

[12] J. Xue, T. Wu, Y. Dai, Y. Xia, *Chem. Rev.* **2019**, *119*, 5298.

[13] L. Persano, A. Camposeo, C. Tekmen, D. Pisignano, *Macro Mol. Mater. Eng.* **2013**, *298*, 504.

[14] a) H. S. SalehHudin, E. N. Mohamad, W. N. L. Mahadi, A. Muhammad Afifi, *Mater. Manuf. Processes* **2018**, *33*, 479; b) A. Khalaf, S. V. Madihally, *Eur. J. Pharm. Biopharm.* **2017**, *112*, 1; c) S. Theron, A. L. Yarin, E. Zussman, E. Kroll, *Polymer* **2005**, *46*, 2889; d) W. Tomaszewski, M. Szadkowski, *Fibres Textiles Eastern Europe* **2005**, *13*, 22; e) A. Varesano, R. A. Carletto, G. Mazzuchetti, *J. Mater. Process. Technol.* **2009**, *209*, 5178; f) A. Varesano, F. Rombaldoni, G. Mazzuchetti, C. Tonin, R. Comotto, *Polym. Int.* **2010**, *59*, 1606.

[15] a) H. El-Sayed, C. Vineis, A. Varesano, S. Mowafi, R. Andrea Carletto, C. Tonetti, M. Abou Taleb, *Nanotechnol. Rev.* **2019**, *8*, 236; b) F. L. Zhou, R. H. Gong, I. Porat, *Polym. Int.* **2009**, *58*, 331.

[16] N. Angel, S. Li, F. Yan, L. Kong, *Trends Food Sci. Technol.* **2022**, *120*, 308.

[17] a) L.-F. Ren, F. Xia, J. Shao, X. Zhang, J. Li, *Desalination* **2017**, *404*, 155; b) J. Cheng, Y. Jun, J. Qin, S.-H. Lee, *Biomaterials* **2017**, *114*, 121.

[18] I. G. Loscertales, A. Barrero, I. Guerrero, R. Cortijo, M. Marquez, A. Ganan-Calvo, *Science* **2002**, *295*, 1695.

[19] a) H. Qu, S. Wei, Z. Guo, *J. Mater. Chem. A* **2013**, *1*, 11513; b) Y. Lu, J. Huang, G. Yu, R. Cardenas, S. Wei, E. K. Wujcik, Z. Guo, *Wiley Interdiscip. Rev.: Nanomed. Nanobiotechnol.* **2016**, *8*, 654.

[20] Y. Dzenis, *Science* **2004**, *304*, 1917.

[21] Y. Li, J. Zhu, H. Cheng, G. Li, H. Cho, M. Jiang, Q. Gao, X. Zhang, *Adv. Mater. Technol.* **2021**, *6*, 2100410.

[22] O. Akampumuza, H. Gao, H. Zhang, D. Wu, X. H. Qin, *Macromol. Mater. Eng.* **2018**, *303*, 1700269.

[23] H. Niu, T. Lin, *J. Nanomater.* **2012**, *2012*, 1.

[24] I. Jahan, L. Wang, X. Wang, *Macromol. Mater. Eng.* **2019**, *304*, 1800588.

[25] J.-H. He, Y. Liu, L. Xu, J.-Y. Yu, G. Sun, *Chaos, Solitons Fractals* **2008**, *37*, 643.

[26] M. Yu, R. H. Dong, X. Yan, G. F. Yu, M. H. You, X. Ning, Y. Z. Long, *Macromol. Mater. Eng.* **2017**, *302*, 1700002.

[27] W. Xia, G. Peng, Y. Hu, G. Dou, *Polym. Eng. Sci.* **2022**, *62*, 247.

[28] L. Wei, R. Sun, C. Liu, J. Xiong, X. Qin, *Mater. Des.* **2019**, *179*, 107885.

[29] G. Zheng, J. Jiang, D. Chen, J. Liu, Y. Liu, J. Zheng, X. Wang, W. Li, J. *Appl. Polym. Sci.* **2019**, *136*, 47574.

[30] R. Zhao, X. Lu, C. Wang, *Compos. Commun.* **2018**, *10*, 140.

[31] J. K. Y. Lee, N. Chen, S. Peng, L. Li, L. Tian, N. Thakor, S. Ramakrishna, *Prog. Polym. Sci.* **2018**, *86*, 40.

[32] a) S. Agarwal, A. Greiner, J. H. Wendorff, *Prog. Polym. Sci.* **2013**, *38*, 963; b) A. Sharma, G. R. Kokil, Y. He, B. Lowe, A. Salam, T. A. Altalhi, Q. Ye, T. Kumeria, *Bioact. Mater.* **2023**, *24*, 535.

[33] Y. Liao, C.-H. Loh, M. Tian, R. Wang, A. G. Fane, *Prog. Polym. Sci.* **2018**, *77*, 69.

[34] a) D. Li, Y. Xia, *Adv. Mater.* **2004**, *16*, 1151; b) J. Xue, J. Xie, W. Liu, Y. Xia, *Acc. Chem. Res.* **2017**, *50*, 1976.

[35] a) C. Luo, M. Nangrejo, M. Edirisinghe, *Polymer* **2010**, *51*, 1654; b) C. Luo, E. Stride, M. Edirisinghe, *Macromolecules* **2012**, *45*, 4669.

[36] O. Husain, W. Lau, M. Edirisinghe, M. Parhizkar, *Mater. Sci. Eng., C* **2016**, *65*, 240.

[37] a) J. Hu, X. Wang, B. Ding, J. Lin, J. Yu, G. Sun, *Macromol. Rapid Commun.* **2011**, *32*, 1729; b) S. Talwar, A. S. Krishnan, J. P. Hinestroza, B. Pourdeyhimi, S. A. Khan, *Macromolecules* **2010**, *43*, 7650.

[38] C. J. Angammana, S. H. Jayaram, *Proc. ESA Annu. Meet. Electrost.* **2010**, *L3*.

[39] N. A. Barakat, M. A. Kanjwal, F. A. Sheikh, H. Y. Kim, *Polymer* **2009**, *50*, 4389.

[40] a) X. Jiang, G. T. Christopherson, H.-Q. Mao, *Interface Focus* **2011**, *1*, 725; b) A. Ardestirajlajimi, S. Farhadian, F. Jamshidi Adegani, S. Mirzaei, M. Soufi Zomorrod, L. Langroudi, A. Doostmohammadi, E. Seyedjafari, M. Soleimani, *Cell Prolif.* **2015**, *48*, 455.

[41] a) S. Jadbabaie, M. Kolahdoozan, F. Naeimi, H. Ebadi-Dehaghani, *RSC Adv.* **2021**, *11*, 30674; b) K. Y. Lee, D. J. Mooney, *Prog. Polym. Sci.* **2012**, *37*, 106.

[42] a) X. Li, B. Cho, R. Martin, M. Seu, C. Zhang, Z. Zhou, J. S. Choi, X. Jiang, L. Chen, G. Walia, J. Yan, M. Callanan, H. Liu, K. Colbert, J. Morrissette-McAlmon, W. Grayson, S. Reddy, J. M. Sacks, H.-Q. Mao, *Sci. Transl. Med.* **2019**, *11*, eaau6210; b) M. D. Davidson, K. H. Song, M.-H. Lee, J. Llewellyn, Y. Du, B. M. Baker, R. G. Wells, J. A. Burdick, *ACS Biomater. Sci. Eng.* **2019**, *5*, 3899.

[43] a) S. Bahrami, A. Solouk, D. Duprez, H. Mirzadeh, *Macromol. Mater. Eng.* **2022**, *307*, 2100584; b) M. S. Karizmeh, S. A. Poursamar, A. Kefayat, Z. Farahbakhsh, M. Rafienia, *Biomater. Adv.* **2022**, *135*, 112667.

[44] T. C. Suh, J. Twiddy, N. Mahmood, K. M. Ali, M. M. Lubna, P. D. Bradford, M. A. Daniele, J. M. Gluck, *ACS Omega* **2022**, *7*, 20006.

[45] a) Y. Li, M. Chen, W. Zhou, S. Gao, X. Luo, L. Peng, J. Yan, P. Wang, Q. Li, Y. Zheng, S. Liu, Y. Cheng, Q. Guo, *Acta Biomater.* **2020**, *113*, 196; b) Y. Ghiyasi, E. Salahi, H. Esfahani, *Mater. Today Commun.* **2021**, *26*, 102163.

[46] a) G. Yan, Z. Yang, J. Li, H. Li, J. Wei, L. Shi, Z. Li, J. Chen, L. Wang, Y. Wu, *Small* **2023**, *19*, 2206403; b) D. Yang, Y. Li, J. Nie, *Carbohydr. Polym.* **2007**, *69*, 538.

[47] L. Jin, T. Wang, Z.-Q. Feng, M. Zhu, M. K. Leach, Y. I. Naim, Q. Jiang, *J. Mater. Chem.* **2012**, *22*, 18321.

[48] N. Nagiah, R. El Khoury, M. H. Othman, J. Akimoto, Y. Ito, D. A. Roberson, B. Joddar, *ACS Omega* **2022**, *7*, 13894.

[49] L. Larrondo, R. St John Manley, *J. Polym. Sci.: Polym. Phys. Ed.* **1981**, *19*, 909.

[50] T. D. Brown, P. D. Dalton, D. W. Hutmacher, *Prog. Polym. Sci.* **2016**, *56*, 116.

[51] F.-L. He, J. He, X. Deng, D.-W. Li, F. Ahmad, Y.-Y. Liu, Y.-L. Liu, Y.-J. Ye, C.-Y. Zhang, D.-C. Yin, *J. Phys. D: Appl. Phys.* **2017**, *50*, 425601.

[52] F. M. Wunner, P. Miesczanek, O. Bas, S. Eggert, J. Maartens, P. D. Dalton, E. M. De-Juan-Pardo, D. W. Hutmacher, *Biofabrication* **2019**, *11*, 025004.

[53] M. Molki, P. Damronglerd, *Heat Transfer Eng.* **2006**, 27, 35.

[54] E. Zhamayev, D. Cho, Y. Lak Joo, *Phys. Fluids* **2011**, 23.

[55] a) S. Laohalertdecha, P. Naphon, S. Wongwises, *Renew. Sustainable Energy Rev.* **2007**, 11, 858; b) E. Zhamayev, H. Zhou, Y. L. Joo, *J. Non-Newtonian Fluid Mech.* **2008**, 153, 95; c) M. Hivet, *J. Electrostat.* **2009**, 67, 222.

[56] P. Dalton, D. Hutmacher, *Chem. An Asian J.* **2011**, 6, 44.

[57] P. D. Dalton, D. Grafahrend, K. Klinkhammer, D. Klee, M. Möller, *Polymer* **2007**, 48, 6823.

[58] S.-S. Choi, S. G. Lee, S. S. Im, S. H. Kim, Y. L. Joo, *J. Mater. Sci. Lett.* **2003**, 22, 891.

[59] J. Geltmeyer, J. De Roo, F. Van den Broeck, J. C. Martins, K. De Buysser, K. De Clerck, *J. Sol-Gel Sci. Technol.* **2016**, 77, 453.

[60] Y. Gu, D. Chen, X. Jiao, *J. Phys. Chem. B* **2005**, 109, 17901.

[61] D. Li, J. T. McCann, Y. Xia, M. Marquez, *J. Am. Ceram. Soc.* **2006**, 89, 1861.

[62] J. Jang, B. G. Hyun, S. Ji, E. Cho, B. W. An, W. H. Cheong, J.-U. Park, *NPG Asia Mater.* **2017**, 9, e432.

[63] X. Wang, B. Ding, B. Li, *Mater. Today* **2013**, 16, 229.

[64] a) W. Nuansing, E. Georgilis, T. V. de Oliveira, G. Charalambidis, A. Eleta, A. G. Coutsolelos, A. Mitraki, A. M. Bittner, *Part. Part. Syst. Charact.* **2014**, 31, 88; b) S. Locarno, A. Eleta-Lopez, M. G. Lupo, M. L. Gelmi, F. Clerici, A. M. Bittner, *RSC Adv.* **2019**, 9, 20565.

[65] M. T. Hunley, A. S. Karikari, M. G. McKee, B. D. Mather, J. M. Layman, A. R. Fornof, T. E. Long, *Macromol. Symp.* **2008**, 270, 1.

[66] a) G. Singh, A. M. Bittner, S. Loscher, N. Malinowski, K. Kern, *Adv. Mater.* **2008**, 20, 2332; b) W. Nuansing, D. Frauchiger, F. Huth, A. Rebollo, R. Hillenbrand, A. M. Bittner, *Faraday Discuss.* **2013**, 166, 209; c) A. S. Tayi, E. T. Pashuck, C. J. Newcomb, M. T. McClendon, S. I. Stupp, *Biomacromolecules* **2014**, 15, 1323.

[67] A. Celebioglu, T. Uyar, *Nanoscale* **2012**, 4, 621.

[68] X. Zhu, Q. Niu, Y. Xu, G. Wu, G. Li, J. Nie, G. Ma, *J. Photochem. Photobiol. A: Chem.* **2018**, 353, 101.

[69] a) D. Li, Y. Xia, *Nano Lett.* **2003**, 3, 555; b) Y. Dai, W. Liu, E. Formo, Y. Sun, Y. Xia, *Polym. Adv. Technol.* **2011**, 22, 326.

[70] P. Viswanathanthamurthi, N. Bhattarai, H. Kim, M. Khil, D. Lee, E.-K. Suh, *J. Chem. Phys.* **2004**, 121, 441.

[71] a) J. E. Efome, D. Rana, T. Matsuura, C. Q. Lan, *J. Mater. Chem. A* **2018**, 6, 4550; b) J. E. Efome, D. Rana, T. Matsuura, C. Q. Lan, *ACS Appl. Mater. Interfaces* **2018**, 10, 18619; c) C.-L. Zhang, S.-H. Yu, *Chem. Soc. Rev.* **2014**, 43, 4423.

[72] T. M. Robinson, D. W. Hutmacher, P. D. Dalton, *Adv. Funct. Mater.* **2019**, 29, 1904664.

[73] C. W. Hull, *United States Patent*, 638905, 1984.

[74] A. Randhawa, S. D. Dutta, K. Ganguly, D. K. Patel, T. V. Patil, K. T. Lim, *Macromol. Biosci.* **2023**, 23, 2200278.

[75] M. Hegde, V. Meenakshisundaram, N. Chartrain, S. Sekhar, D. Tafti, C. B. Williams, T. E. Long, *Adv. Mater.* **2017**, 29, 1701240.

[76] Y. Shao, Z. Liao, B. Gao, B. He, *ACS Omega* **2022**, 7, 11530.

[77] D. Ahn, L. M. Stevens, K. Zhou, Z. A. Page, *ACS Cent. Sci.* **2020**, 6, 1555.

[78] C. Tew, L. Hornbeck, J. Lin, E. Chiu, K. Kornher, J. Conner, K. Komatsuzaki, P. Urbanus, presented at Proceedings of IEEE Int. Solid-State Circuits Conf.-ISSCC'94, San Francisco, CA, USA, February 1994.

[79] M. M. Rahman, Texas Tech University, 2002.

[80] J. Wang, Y. Liu, X. Qian, X. Ma, *Chem. Reagents* **2018**, 40, 528.

[81] L. Wu, L. Zhao, M. Jian, Y. Mao, M. Yu, X. Guo, *Rapid Prototyping J.* **2018**, 24, 1500.

[82] D. G. Chang, S. Li, C. F. An, *Adv. Mater. Res.* **2012**, 426, 163.

[83] a) X. Li, B. Liu, B. Pei, J. Chen, D. Zhou, J. Peng, X. Zhang, W. Jia, T. Xu, *Chem. Rev.* **2020**, 120, 10793; b) L. Moroni, T. Boland, J. A. Burdick, C. De Maria, B. Derby, G. Forgacs, J. Groll, Q. Li, J. Maldá, V. A. Mironov, *Trends Biotechnol.* **2018**, 36, 384.

[84] a) M. A. Heinrich, W. Liu, A. Jimenez, J. Yang, A. Akpek, X. Liu, Q. Pi, X. Mu, N. Hu, R. M. Schiffelers, *Small* **2019**, 15, 1805510; b) C. Mandrycky, Z. Wang, K. Kim, D.-H. Kim, *Biotechnol. Adv.* **2016**, 34, 422.

[85] B. Derby, *Ann. Rev. Mater. Res.* **2010**, 40, 395.

[86] a) H. Gudapati, M. Dey, I. Ozbolat, *Biomaterials* **2016**, 102, 20; b) J. Jiang, G. Shea, P. Rastogi, T. Kamperman, C. H. Venner, C. W. Visser, *Adv. Mater.* **2021**, 33, 2006336.

[87] a) J. Li, F. Rossignol, J. Macdonald, *Lab Chip* **2015**, 15, 2538; b) I. Matai, G. Kaur, A. Seyedehsaei, A. McClinton, C. T. Laurencin, *Biomaterials* **2020**, 226, 119536.

[88] R. E. Saunders, J. E. Gough, B. Derby, *Biomaterials* **2008**, 29, 193.

[89] H. Wijshoff, *Phys. Rep.* **2010**, 491, 77.

[90] W. L. Ng, J. M. Lee, W. Y. Yeong, M. W. Naing, *Biomater. Sci.* **2017**, 5, 632.

[91] Y. Jiang, M. N. Islam, R. He, X. Huang, P. F. Cao, R. C. Advincula, N. Dahotre, P. Dong, H. F. Wu, W. Choi, *Adv. Mater. Technol.* **2023**, 8, 2200492.

[92] J. Zhang, P. Xiao, *Poly. Chem.* **2018**, 9, 1530.

[93] J. Palaganas, A. C. de Leon, J. Mangadlao, N. Palaganas, A. Mael, Y. J. Lee, H. Y. Lai, R. Advincula, *Macromol. Mater. Eng.* **2017**, 302, 1600477.

[94] J. Zhang, P. Xiao, *Polym. Chem.* **2018**, 9, 1530.

[95] Q. Zhang, X. Wang, G. Kuang, Y. Yu, Y. Zhao, *Sci. Bull.* **2020**, 65, 380.

[96] A. Oesterreicher, J. Wiener, M. Roth, A. Moser, R. Gmeiner, M. Edler, G. Pinter, T. Griesser, *Polym. Chem.* **2016**, 7, 5169.

[97] T. Wirth, in *Microreactors in Organic Chemistry and Catalysis*, John Wiley & Sons, New Jersey, USA 2013.

[98] a) A. Bertsch, S. Jiguet, P. Renaud, J. *Micromech. Microeng.* **2003**, 14, 197; b) M. Schwentenwein, J. Homa, *Int. J. Appl. Ceram. Technol.* **2015**, 12, 1.

[99] P. Colombo, G. Mera, R. Riedel, G. D. Soraru, *J. Am. Ceram. Soc.* **2010**, 93, 1805.

[100] J. R. Woodard, A. J. Hilldore, S. K. Lan, C. Park, A. W. Morgan, J. A. C. Eurell, S. G. Clark, M. B. Wheeler, R. D. Jamison, A. J. W. Johnson, *Biomaterials* **2007**, 28, 45.

[101] a) M. L. Griffith, J. W. Halloran, *J. Am. Ceram. Soc.* **1996**, 79, 2601; b) H. Yves-Christian, W. Jan, M. Wilhelm, W. Konrad, P. Reinhart, *Phys. Procedia* **2010**, 5, 587; c) D. T. Pham, R. S. Gault, *Int. J. Machine Tools Manuf.* **1998**, 38, 1257.

[102] D. Aza, L. Martinez, A. Guitian, D. Aza, *J. Microscopy* **2000**, 197, 60.

[103] a) P. Siriphannont, Y. Kameshima, A. Yasumori, K. Okada, S. Hayashi, *J. Biomed. Mater. Res.* **2000**, 52, 30; b) T. Kokubo, H. Takadama, *Biomaterials* **2006**, 27, 2907; c) S. Xu, K. Lin, Z. Wang, J. Chang, L. Wang, J. Lu, C. Ning, *Biomaterials* **2008**, 29, 2588.

[104] a) S. Bose, S. Vahabzadeh, A. Bandyopadhyay, *Mater. Today* **2013**, 16, 496; b) P. X. Lan, J. W. Lee, Y.-J. Seol, D.-W. Cho, *J. Mater. Sci.: Mater. Med.* **2009**, 20, 271.

[105] a) Y. Song, K. Lin, S. He, C. Wang, S. Zhang, D. Li, J. Wang, T. Cao, L. Bi, G. Pei, *Int. J. Nanomed.* **2018**, 13, 505; b) Y. Chen, J. Song, S. Wang, W. Liu, *Macromol. Biosci.* **2021**, 21, 2100147.

[106] C. Lin, J. Lv, Y. Li, F. Zhang, J. Li, Y. Liu, L. Liu, J. Leng, *Adv. Funct. Mater.* **2019**, 29, 1906569.

[107] a) S. A. Park, S. J. Lee, J. M. Seok, J. H. Lee, W. D. Kim, I. K. Kwon, *J. Bionic Eng.* **2018**, 15, 435; b) S. Zhang, X. Shi, Z. Miao, H. Zhang, X. Zhao, K. Wang, J. Qin, G. Zhang, *Adv. Eng. Mater.* **2022**, 24, 2101134.

[108] Y. Yang, D. Lei, S. Huang, Q. Yang, B. Song, Y. Guo, A. Shen, Z. Yuan, S. Li, F. L. Qing, *Adv. Healthcare Mater.* **2019**, 8, 1900065.

[109] Q. Lei, J. He, D. Li, *Nanoscale* **2019**, 11, 15195.

[110] A. Azarni, K. E. Lafin, M. Jamal, R. Fernandes, D. H. Gracias, *Biomed. Microdevices* **2011**, 13, 51.

[111] M. Zarek, N. Mansour, S. Shapira, D. Cohn, *Macromol. Rapid Commun.* **2017**, 38, 1600628.

[112] A. Y. Lee, J. An, C. K. Chua, *Engineering* **2017**, 3, 663.

[113] a) Y. Yang, Y. Chen, Y. Wei, Y. Li, *Int. J. Adv. Manuf. Technol.* **2016**, *84*, 2079; b) Z. Ding, C. Yuan, X. Peng, T. Wang, H. J. Qi, M. L. Dunn, *Sci. Adv.* **2017**, *3*, 1602890; c) M. Zarek, M. Layani, I. Cooperstein, E. Sachyani, D. Cohn, S. Magdassi, *Adv. Mater.* **2016**, *28*, 4449.

[114] J. Wu, C. Yuan, Z. Ding, M. Isakov, Y. Mao, T. Wang, M. L. Dunn, H. J. Qi, *Sci. Rep.* **2016**, *6*, 24224.

[115] E. Sachyani Keneth, A. Kamyshny, M. Totaro, L. Beccai, S. Magdassi, *Adv. Mater.* **2021**, *33*, 2003387.

[116] Q. Ge, A. H. Sakhaei, H. Lee, C. K. Dunn, N. X. Fang, M. L. Dunn, *Sci. Rep.* **2016**, *6*, 31110.

[117] Q. Zhang, X. Wang, G. Kuang, Y. Yu, Y. Zhao, *Research* **2022**, *2022*, 9784510.

[118] M. Layani, X. Wang, S. Magdassi, *Adv. Mater.* **2018**, *30*, 1706344.

[119] N. W. Pensa, A. S. Curry, P. P. Bonvallet, N. F. Bellis, K. M. Rettig, M. S. Reddy, A. W. Eberhardt, S. L. Bellis, *Biomater. Res.* **2019**, *23*, 1.

[120] J. Yoo, J. H. Park, Y. W. Kwon, J. J. Chung, I. C. Choi, J. J. Nam, H. S. Lee, E. Y. Jeon, K. Lee, S. H. Kim, *Biomater. Sci.* **2020**, *8*, 6261.

[121] S.-J. Lee, M. Nowicki, B. Harris, L. G. Zhang, *Tissue Eng., Part A* **2017**, *23*, 491.

[122] a) M. Centola, A. Rainer, C. Spadaccio, S. De Porcellinis, J. Genovese, M. Trombetta, *Biofabrication* **2010**, *2*, 014102. b) H.-J. Ahn, R. Khalmuratova, S. A. Park, E.-J. Chung, H.-W. Shin, S. K. Kwon, *Tissue Eng. Regener. Med.* **2017**, *14*, 631.

[123] S. J. Lee, J. S. Choi, M. R. Eom, H. H. Jo, I. K. Kwon, S. K. Kwon, S. A. Park, *Nanoscale* **2020**, *12*, 4846.

[124] a) A. B. Touré, E. Mele, J. K. Christie, *Nanomaterials* **2020**, *10*, 626; b) D. Qi, S. Wu, H. Lin, M. A. Kuss, Y. Lei, A. Krasnoslobodtsev, S. Ahmed, C. Zhang, H. J. Kim, P. Jiang, *ACS Appl. Mater. Interfaces* **2018**, *10*, 21825; c) C. Mota, S. Danti, D. D'Alessandro, L. Trombi, C. Ricci, D. Puppi, D. Dinucci, M. Milazzo, C. Stefanini, F. Chiellini, *Biofabrication* **2015**, *7*, 025005; d) H. Sanie, S. Mousavi, *Polymer* **2020**, *196*, 122467; e) I. Rajzer, A. Kurowska, A. Jabłoński, S. Jatteau, M. Śliwka, M. Ziąbka, E. Menasze, *Mater. Des.* **2018**, *155*, 297.

[125] a) Z. Yang, Z. Song, X. Nie, K. Guo, Y. Gu, *Stem cell Res. Ther.* **2020**, *11*, 1; b) S. Naghieh, E. Foroozehmehr, M. Badrossamay, M. Kharaziha, *Mater. Des.* **2017**, *133*, 128; c) N. Maurmann, D. P. Pereira, D. Burguez, F. D. de S Pereira, P. I. Neto, R. A. Rezende, D. Gamba, J. V. da Silva, P. Pranke, *Biomed. Phys. Engin. Exp.* **2017**, *3*, 045005; d) B. Huang, E. Aslan, Z. Jiang, E. Daskalakis, M. Jiao, A. Aldalbahi, C. Vyas, P. Bártolo, *Addit. Manuf.* **2020**, *36*, 101452; e) J.-S. Lee, S. Chae, D. Yoon, D. Yoon, W. Chun, G. H. Kim, *Biofabrication* **2020**, *12*, 045028; f) T. Maver, D. Smrke, M. Kurečić, L. Gradišnik, U. Maver, K. S. Kleinschek, *J. Sol-Gel Sci. Technol.* **2018**, *88*, 33.

[126] N. Kasoju, J. George, H. Ye, Z. Cui, *Nanomaterials* **2018**, *8*, 863.

[127] B. Freystetter, M. Grab, L. Grefen, L. Bischof, L. Isert, P. Mela, D. Bezuidenhout, C. Hagl, N. Thierfelder, *JoVE (J. Visual. Exp.)* **2022**, *181*, 63604.

[128] S. Liu, Z. Wang, X. Chen, M. Han, J. Xu, T. Li, L. Yu, M. Qin, M. Long, M. Li, H. Zhang, Y. Li, L. Wang, W. Huang, Y. Wu, *Adv. Healthcare Mater.* **2023**, *12*, 2300719.

[129] M. Zhu, J. Tan, L. Liu, J. Tian, L. Li, B. Luo, C. Zhou, L. Lu, *Mater. Sci. Eng., C* **2021**, *128*, 112310.

[130] M. Yeo, G. Kim, *Acta Biomater.* **2020**, *107*, 102.

[131] H. Chen, H. Zhang, Y. Shen, X. Dai, X. Wang, K. Deng, X. Long, L. Liu, X. Zhang, Y. Li, *Front. Bioengin. Biotechnol.* **2021**, *9*, 684105.

[132] R. M. Clohessy, D. J. Cohen, K. Stumbaite, B. D. Boyan, Z. Schwartz, *J. Biomed. Mater. Res., Part B* **2020**, *108*, 2560.

[133] Y. Kang, C. Wang, Y. Qiao, J. Gu, H. Zhang, T. Peijs, J. Kong, G. Zhang, X. Shi, *Biomacromolecules* **2019**, *20*, 1765.

[134] Y. Yu, S. Hua, M. Yang, Z. Fu, S. Teng, K. Niu, Q. Zhao, C. Yi, *RSC Adv.* **2016**, *6*, 110557.

[135] B. Qiu, X. Chen, F. Xu, D. Wu, Y. Zhou, W. Tu, H. Jin, G. He, S. Chen, D. Sun, *Microsyst. Nanoeng.* **2022**, *8*, 102.

[136] L.-C. Kong, H. A. Li, Q.-L. Kang, G. Li, *J. Orthop. Trans.* **2020**, *25*, 3.

[137] N. Su, C. Villicana, F. Yang, *Biomaterials* **2022**, *286*, 121604.

[138] S. Irandoost, S. Müftü, *Sci. Rep.* **2020**, *10*, 4335.

[139] B. Sun, M. Lian, Y. Han, X. Mo, W. Jiang, Z. Qiao, K. Dai, *Bioactive Mater.* **2021**, *6*, 179.

[140] Z. Wang, Y. Wang, J. Yan, K. Zhang, F. Lin, L. Xiang, L. Deng, Z. Guan, W. Cui, H. Zhang, *Adv. Drug Delivery Rev.* **2021**, *174*, 504.

[141] M. Geng, Q. Zhang, J. Gu, J. Yang, H. Du, Y. Jia, X. Zhou, C. He, *Biomater. Sci.* **2021**, *9*, 2631.

[142] X. Zhou, Y. Qian, L. Chen, T. Li, X. Sun, X. Ma, J. Wang, C. He, *ACS Nano* **2023**, *17*, 5140.

[143] J. He, J. Fang, P. Wei, Y. Li, H. Guo, Q. Mei, F. Ren, *Acta Biomater.* **2021**, *121*, 665.

[144] a) X. Ye, L. Lu, M. E. Kolewe, K. Hearon, K. M. Fischer, J. Coppeta, L. E. Freed, *Adv. Mater.* **2014**, *26*, 7202; b) P. Blinder, P. S. Tsai, J. P. Kaufhold, P. M. Knutson, H. Suhl, D. Kleinfeld, *Nat. Neurosci.* **2013**, *16*, 889.

[145] R. Jain, *Nat. Biotechnol.* **2005**, *23*, 821.

[146] I. Cicha, R. Detsch, R. Singh, S. Reakasame, C. Alexiou, A. R. Boccaccini, *Curr. Opin. Biomed. Eng.* **2017**, *2*, 83.

[147] D. Lei, Y. Yang, Z. Liu, B. Yang, W. Gong, S. Chen, S. Wang, L. Sun, B. Song, H. Xuan, *Mater. Horiz.* **2019**, *6*, 1197.

[148] T. Fukunishi, C. A. Best, T. Sugiura, J. Opfermann, C. S. Ong, T. Shinoka, C. K. Breuer, A. Krieger, J. Johnson, N. Hibino, *J. Thorac. Cardiovasc. Surg.* **2017**, *153*, 924.

[149] S. Vijayaventaraman, W. Lu, J. Fuh, *Biofabrication* **2016**, *8*, 032001.

[150] P. I. Morgado, A. Aguiar-Ricardo, I. J. Correia, *J. Membr. Sci.* **2015**, *490*, 139.

[151] H. Yoon, J.-S. Lee, H. Yim, G. Kim, W. Chun, *RSC Adv.* **2016**, *6*, 21439.

[152] J. I. Kim, C. S. Kim, *ACS Appl. Mater. Interfaces* **2018**, *10*, 12390.

[153] D. Gao, Z. Wang, Z. Wu, M. Guo, Y. Wang, Z. Gao, P. Zhang, Y. Ito, *Mater. Sci. Eng., C* **2020**, *112*, 110942.

[154] S. P. Miguel, C. S. Cabral, A. F. Moreira, I. J. Correia, *Colloids Surf., B* **2019**, *181*, 994.

[155] K. Solowiej, D. Upton, *Nursing Times* **2010**, *106*, 21.

[156] A. D. Theocharis, S. S. Skandalis, C. Gialeli, N. K. Karamanos, *Adv. Drug Delivery Rev.* **2016**, *97*, 4.

[157] M. Protasoni, S. Sangiorgi, A. Cividini, G. T. Culuvaris, G. Tomei, C. Dell'Orbo, M. Raspanti, S. Balbi, M. Reguzzoni, *J. Neurosurg.* **2011**, *114*, 1723.

[158] Y. Xu, G. Shi, J. Tang, R. Cheng, X. Shen, Y. Gu, L. Wu, K. Xi, Y. Zhao, W. Cui, L. Chen, *Sci. Adv.* **2020**, *6*, eabc2036.

[159] a) L. Gao, M. E. Kupfer, J. P. Jung, L. Yang, P. Zhang, Y. Da Sie, Q. Tran, V. Ajeti, B. T. Freeman, V. G. Fast, *Circ. Res.* **2017**, *120*, 1318; b) M. Kitsara, O. Agbulut, D. Kontziampasis, Y. Chen, P. Menasché, *Acta Biomater.* **2017**, *48*, 20.

[160] M. Mao, X. Qu, Y. Zhang, B. Gu, C. Li, R. Liu, X. Li, H. Zhu, J. He, D. Li, *Nat. Commun.* **2023**, *14*, 2077.

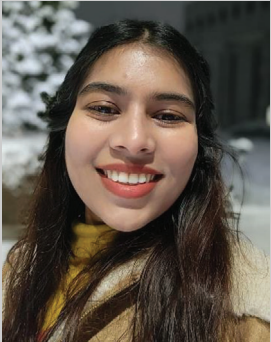
[161] J. R. Gershak, S. Hernandez, G. Fontana, L. R. Perreault, K. J. Hansen, S. A. Larson, B. Y. Binder, D. M. Dolivo, T. Yang, T. Dominko, *Biomaterials* **2017**, *125*, 13.

[162] M. Mao, H. P. Bei, C. H. Lam, P. Chen, S. Wang, Y. Chen, J. He, X. Zhao, *Small* **2020**, *16*, 2000546.

[163] a) B. M. Baker, B. Trappmann, W. Y. Wang, M. S. Sakar, I. L. Kim, V. B. Shenoy, J. A. Burdick, C. S. Chen, *Nat. Mater.* **2015**, *14*, 1262; b) M. S. Hall, F. Alisafaei, E. Ban, X. Feng, C.-Y. Hui, V. B. Shenoy, M. Wu, *Proc. Natl. Acad. Sci. U. S. A.* **2016**, *113*, 14043.

[164] C. Zhi, S. Shi, Y. Si, B. Fei, H. Huang, J. Hu, *Adv. Mater. Technol.* **2023**, *8*, 2201161.

[165] M. E. Prendergast, J. A. Burdick, *Adv. Mater.* **2020**, *32*, 1902516.



Ayushi Randhawa is a doctoral student in Biosystems Engineering at Kangwon National University, South Korea. She received her Master's degree from Bangalore University, India. Her research interest is developing stimuli-dependent regenerative therapies for healing damaged tissues.



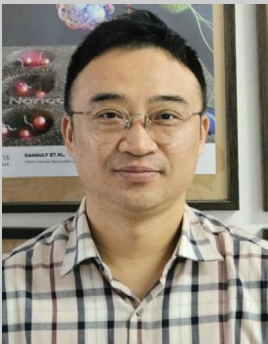
Sayan Deb Dutta is a Postdoctoral Research Associate at Kangwon National University. He received his doctoral degree from the Department of Biosystems Engineering at Kangwon National University, South Korea. He reviewed his Master's degree from the University of Kalyani, India. His research interest is the synthesis of multifunctional nanomaterials for 3D printing and nanotheranostic applications for tissue engineering.



Keya Ganguly is a Postdoctoral Research Associate at Kangwon National University. She received her doctoral degree from the Department of Biosystems Engineering at Kangwon National University, South Korea. She received her Master's degree from Presidency University, India. Her research interest is developing a multi-stimuli-assisted scaffolding platform for tissue engineering and biosensing.



Tejal V. Patil is a doctoral student of Biosystems Engineering at Kangwon National University, South Korea. She received her Master's degree from the Institute of Chemical Technology, Mumbai, India. Her research interest is developing biomaterials for application in bacteria eradication and tissue regeneration.



Ki-Taek Lim is a professor at the Department of Biosystems Engineering at Kangwon National University, South Korea. He received his doctoral degree from Seoul National University, South Korea, and joined as a postdoctoral research fellow at the University of Arkansas, USA. He has a strong knowledge of mechatronics and regenerative medicines. His research focuses on developing the bio-nanorobotics system with novel bioreactors and stem cell cultures for tissue-engineering applications.